arXiv:1212.4768v3 [hep-lat] 16 May 2013

Lattice QCD ensembles with four flavors of highly improved staggered quarks

A. Bazavov

Physics Department, Brookhaven National Laboratory, Upton, NY 11973, USA

C. Bernard and J. Komijani

Department of Physics, Washington University, St. Louis, MO 63130, USA

C. DeTar and L. Levkova*

Department of Physics and Astronomy,
University of Utah, Salt Lake City, UT 84112, USA

W. Freeman

Department of Physics, The George Washington University, Washington, DC 20052, USA

Steven Gottlieb and Ran Zhou

Department of Physics, Indiana University, Bloomington, IN 47405, USA

U.M. Heller

American Physical Society, One Research Road, Ridge, NY 11961, USA

J.E. Hetrick

Physics Department, University of the Pacific, Stockton, CA 95211, USA

J. Laiho

Department of Physics and Astronomy,
University of Glasgow, Glasgow G12 8GG, Scotland, UK

J. Osborn

Argonne Leadership Computing Facility,
Argonne National Laboratory, Argonne, IL 60439, USA

---

* present address: Department of Physics, University of Arizona, Tucson, AZ 85721, USA

R.L. Sugar

Department of Physics, University of California, Santa Barbara, CA 93106, USA

D. Toussaint

Department of Physics, University of Arizona, Tucson, AZ 85721, USA

R.S. Van de Water

Theoretical Physics Department, Fermi National

Accelerator Laboratory, Batavia 60510, USA

[MILC Collaboration]

(Dated: May 17, 2013)

Abstract

We present results from our simulations of quantum chromodynamics (QCD) with four flavors of quarks: u, d, s, and c. These simulations are performed with a one-loop Symanzik improved gauge action, and the highly improved staggered quark (HISQ) action. We are generating gauge configurations with four values of the lattice spacing ranging from 0.06 fm to 0.15 fm, and three values of the light quark mass, including the value for which the Goldstone pion mass is equal to the physical pion mass. We discuss simulation algorithms, scale setting, taste symmetry breaking, and the autocorrelations of various quantities. We also present results for the topological susceptibility which demonstrate the improvement of the HISQ configurations relative to those generated earlier with the asqtad improved staggered action.

PACS numbers: 12.38.Gc

I. INTRODUCTION

Over the past decade, we have generated a large library of gauge configuration ensembles with three flavors of improved staggered (asqtad) quarks [1]. These ensembles are publicly available, and they are being used by our group and several others to study a wide variety of problems in high-energy and nuclear physics [1]. A number of the most challenging problems that we and other lattice gauge theorists are pursuing, however, require a level of precision that is beyond the reach of the current asqtad ensembles, and generating additional ones with smaller lattice spacings and lighter up and down quark masses would be very computationally expensive. We have therefore begun generating a new library of gauge configuration ensembles using the highly improved staggered quark (HISQ) action introduced by the HPQCD Collaboration [2–4]. In this paper, we describe the ensembles produced to date, and report on the initial calculations performed with them.

The HPQCD Collaboration developed the HISQ action to reduce the taste-symmetry violations associated with staggered quarks, and to improve the quark dispersion relation sufficiently so that charm quarks can be simulated at lattice spacings accessible with today's computers. They tested the new action using HISQ valence quarks on quenched gauge configurations and on ones we had generated with asqtad sea quarks [2–4]. More recently, they have obtained impressive results for charm and heavy-light physics again using HISQ valence quarks on asqtad configurations [5–13]. We have performed tests of scaling in the lattice spacing using HISQ valence quarks with gauge configurations generated with HISQ sea quarks [14]. We found that lattice artifacts for the HISQ action are reduced by approximately a factor of three from those of the asqtad action for the same lattice spacing, and taste splittings in the pion masses are reduced sufficiently to enable us to undertake simulations with the mass of the Goldstone pion at or near the physical pion mass. Moreover, the improvement in the quark dispersion relation enables us to include charm sea quarks in the simulations.

Given the successes of the HISQ action, we have embarked on a project to generate ensembles of gauge configurations using it along with a one-loop Symanzik improved gauge action [15]. We are working at four different lattice spacings, $a \approx 0.06$, 0.09, 0.12 and 0.15 fm, in order to control extrapolations to the continuum limit. We include up, down, strange, and charm sea quarks. For most ensembles, the masses of the strange and charm

$\approx a$ (fm)	m_l/m_s	$N_s^3 \times N_t$	$M_\pi L$	M_π (MeV)	N_{lats}
0.15	1/5	$16^3 \times 48$	3.78	306.9(5)	1021
0.15	1/10	$24^3 \times 48$	3.99	214.5(2)	1000
0.15	1/27	$32^3 \times 48$	3.30	131.0(1)	1020
0.12	1/5	$24^3 \times 64$	4.54	305.3(4)	1040
0.12	1/10	$24^3 \times 64$	3.22	218.1(4)	1020
0.12	1/10	$32^3 \times 64$	4.29	216.9(2)	1000
0.12	1/10	$40^3 \times 64$	5.36	217.0(2)	1029
0.12	1/27	$48^3 \times 64$	3.88	131.7(1)	1000
0.09	1/5	$32^3 \times 96$	4.50	312.7(6)	1011
0.09	1/10	$48^3 \times 96$	4.71	220.3(2)	1000
0.09	1/27	$64^3 \times 96$	3.66	128.2(1)	235+467
0.06	1/5	$48^3 \times 144$	4.51	319.3(5)	1000
0.06	1/10	$64^3 \times 144$	4.25	229.2(4)	435+227
0.06	1/27	$96^3 \times 192$	3.95	135.5(2)	240

TABLE I: HISQ gauge configuration ensembles with strange and charm quark masses set at or very close to their physical values. The first column gives the lattice spacing for which we were aiming, which in all cases turned out to be a good approximation to the actual lattice spacing that could only be determined after the lattices were created. The second column gives the ratio of the simulation mass of the light quark to the physical mass of the strange quark, the third the lattice dimensions, the fourth the product of the Goldstone pion mass and the spatial extent of the lattice, and the fifth the Goldstone pion mass in MeV. The pion masses were converted to physical units using the f_{p4s} scale setting described in section III. The quoted errors include only the statistical errors on the pion mass and f_{p4s} in lattice units in the individual ensemble; they do not include systematic errors such as the errors on the physical values of f_{p4s} in Table VII. The sixth column gives the number of equilibrated gauge configurations. Where the sixth column is the sum of two numbers, these are the numbers of lattices generated with the RHMC and RHMD algorithms respectively, as discussed in section II. We plan to save approximately 1,000 configurations in each ensemble, so those for which $N_{lats} \geq 1,000$ are considered to be complete.

m_{l1}/m_s	m_{l2}/m_s	m'_s/m_s	$N_s^3 \times N_t$	N_{lats}
0.10	0.10	0.10	$32^3 \times 64$	1020
0.10	0.10	0.25	$32^3 \times 64$	1020
0.10	0.10	0.45	$32^3 \times 64$	1020
0.10	0.10	0.60	$32^3 \times 64$	1020
0.25	0.25	0.25	$24^3 \times 64$	1020
0.20	0.20	0.60	$24^3 \times 64$	1020
0.175	0.175	0.45	$32^3 \times 64$	1020
0.10	0.25	0.45	$32^3 \times 64$	1020

TABLE II: HISQ gauge configuration ensembles with lighter-than-physical strange quark masses. All ensembles have a lattice spacing of $a \approx 0.12$ fm and charm-quark mass as close as possible to its physical value. The first two columns give the ratio of the light quark masses to the physical strange quark mass. (We distinguish between the masses of the two light quarks because in the ensemble in the last row they are different.) The third column gives the ratio of the simulation strange-quark mass to the physical strange-quark mass, and the fourth column shows the lattice dimensions. The fifth shows the number of equilibrated configurations.

quarks, m_s and m_c, respectively, are fixed at their physical values. For these ensembles, the up and down quark masses are taken to be degenerate with a common mass m_l, which has a negligible effect ($< 1\%$) on isospin-averaged quantities. We are generating configurations with three values of the light quark mass: $m_l = m_s/5$, $m_s/10$, and the value such that the Goldstone pion mass is as close as possible to the physical pion mass, which is approximately $m_s/27$. Table I shows the current state of these ensembles. Prior to the simulations, the lattice spacing and the physical values of the quark masses can only be estimated. Their precise values are outputs from the analysis described later in this paper. Note that we have generated three ensembles with $a \approx 0.12$ fm and $m_l = m_s/10$ that differ only in their spatial volumes. The purpose of using three different volumes is to enable tests of finite-size effects. The factor governing such effects, $e^{-M_\pi L}$, varies by a factor of eight over this range of spatial sizes, so we expect to have a sufficient lever arm for these tests. In Table III, we compare the values of the plaquette, the strange and light quark condensates, and r_1/a on

these three lattices. A comparison of finite size effects for the pion and kaon masses and leptonic decay constants on these configurations with the predictions of chiral perturbation theory can be found in Ref. [16].

	$L = 24$	$L = 32$	$L = 40$
Plaquette	0.556621(7)	0.556631(5)	0.556623(3)
$\bar{\psi}\psi_l$	0.016957(33)	0.017020(18)	0.017068(13)
$\bar{\psi}\psi_s$	0.061764(18)	0.061719(12)	0.061735(8)
r_1/a	2.585(19)	2.626(13)	2.611(9)

TABLE III: Effects of spatial size in the $a \approx 0.12$ fm $m_l = m_s/5$ ensembles, which differ only in the spatial size of the lattices. $\bar{\psi}\psi$ is in units of the lattice spacing, and is shown for both the light quark and strange quark masses. Values for r_1/a come from a fit to the heavy-quark potential over spatial separations from 1.5 to 4.0, and time lengths 5 to 7.

With the HISQ action, as with less improved staggered fermion actions, each lattice fermion species corresponds to four "tastes" of fermions in the continuum limit. To eliminate the three unwanted tastes from the quark sea, we use the fourth-root procedure for each of the sea-quark flavors, up, down, strange, and charm. For numerical and theoretical arguments justifying this fourth-root procedure we refer the reader to Refs. [17] and [18].

We have also generated a limited number of ensembles with the strange-quark mass lighter than its physical value, because including such ensembles has proven very useful in controlling chiral extrapolations of physical quantities. In one of those ensembles, we also chose different values for the two light-quark masses, up and down, to probe for isospin-breaking effects. These ensembles are listed in Table II.

We note that even though we are generating some ensembles with the Goldstone pion mass at the physical value and with the strange quark mass near its physical value, controlling the chiral expansion using a variety of other ensembles with different quark masses is still very useful for several reasons: (1) The lattice spacing and the physical values of the quark masses can only be estimated prior to the simulations. Their precise values are outputs from a detailed analysis made after the ensembles have been created in which the unphysical light- and strange-quark mass ensembles play important roles. (2) We can both determine the dependence on the strange sea-quark mass and extrapolate to the limit where that mass

vanishes, which is important for studies of a variety of physical quantities. (3) Since the continuum and chiral expansions are closely connected through staggered chiral perturbation theory, controlling the chiral expansion helps us to take the continuum limit with small extrapolation errors. (4) Statistical fluctuations of physical quantities with up and down sea and valence masses at their physical values tend to be larger than at somewhat higher masses, so including higher-mass ensembles in a chiral fit can significantly decrease the final errors. (5) Having a range of strange and light sea-quark masses allows us to determine low-energy constants of the chiral expansion, which are important fundamental parameters of QCD in their own right.

The details of our simulations and their present status are given in Sec. II. In this section, we also compare configurations generated with the RHMC and RHMD algorithms. Although we have used the former for nearly all the ensembles produced to date, at the smallest lattice spacings the gauge fields appear to be smooth enough to use the latter, which leads to a significant savings in computer time. Scale setting is addressed in Sec. III, where we give results based both on the Sommer parameter r_1 [19, 20] and on the decay constants of (fictitious) pseudoscalar mesons [21]. In Sec. IV, we present results for the topological susceptibility of the QCD vacuum obtained from the HISQ ensembles. Tunneling between different topological sectors appears to be sufficient for them to equilibrate. The topological susceptibility provides a particularly stringent test of the HISQ gauge configurations because it is computed from them without involving valence quarks. Thus, comparison of the topological susceptibility on the asqtad and HISQ configurations directly demonstrates the improvement in the gauge configurations. In Sec. V, we discuss taste-symmetry violations in the light-light, heavy-light and heavy-heavy pseudoscalar sectors, and demonstrate the improvement in the light-light sector provided by the HISQ action, while in Sec. VI, we discuss autocorrelation times for a variety of physical variables. In Sec. VII, we present our conclusions, and in an appendix, we tabulate the taste-symmetry breaking pseudoscalar meson mass splittings, which can be used in the staggered chiral perturbation theory analysis of masses and matrix elements on these ensembles.

II. SIMULATIONS

The details of our simulations were given in Ref. [14]. Here we briefly outline our approach in order to make this paper self-contained. We are using a one-loop Symanzik improved gauge action [15] and the HISQ action [2–4]. The gauge action includes 1×1 and 1×2 planar Wilson loops, and a $1 \times 1 \times 1$ "parallelogram". The coefficients of these terms are calculated perturbatively, and are then tadpole improved. They include both one-gluon-loop and one-quark-loop contributions [22]. The HISQ action consists of a Fat7 smearing of the gauge links, then a projection of each smeared link onto a unitary matrix, followed by an "asq" smearing with twice the Lepage term and including the Naik term, a third nearest-neighbor coupling. This is designed to ensure that the quark action is order a^2 improved. The use of two levels of smearing produces a smooth gauge field seen by the quarks, which leads to the reduction in taste-symmetry violations mentioned previously. Finally, a modification of the Naik term [4] improves the dispersion relation of the charm quark sufficiently that it can be included in our simulations.

We have used the rational hybrid Monte Carlo (RHMC) algorithm [23] to generate configurations with two exceptions discussed below. We use different molecular dynamics step sizes for the gauge and fermion parts of the action, with three gauge steps for each fermion one [24]. The Omelyan integration algorithm is employed for both the gauge and fermion parts of the action [24, 25], and five pseudofermion fields are used, each with a rational function approximation for the fractional powers of the fermion determinants. The projection of links onto U(3) after the Fat7 smearing can lead to spikes in the fermion force, which give rise to low acceptance rates, especially on coarse lattices. These spikes are smoothed out by means of a guiding Hamiltonian in the molecular dynamics evolution [14], and the algorithm is made exact by means of a Metropolis accept/reject step at the end of each trajectory, which employs the exact Hamiltonian.

The simulation parameters for the ensembles with physical strange-quark mass are given in Table IV, and those for ensembles with lighter-than-physical strange quarks in Table V.

Obtaining a good acceptance rate with the RHMC algorithm requires a step size small enough that the change in the action over a trajectory is of order one, and on large lattices this requires a small simulation time step. However, this requirement is unphysical in the sense that we are interested in intensive quantities, not extensive ones. In our earlier series

$10/g^2$	am_l	am_s	am_c	u_0	ϵ_N	s	len.	ϵ	acc.
5.80	0.013	0.065	0.838	0.85535	-0.3582*	5	1.0	0.033	0.73
5.80	0.0064	0.064	0.828	0.85535	-0.3484	5	1.0	0.020	0.71
5.80	0.00235	0.0647	0.831	0.85535	-0.3503	5	0.5	0.018	0.68
6.00	0.0102	0.0509	0.635	0.86372	-0.2308*	5	1.0	0.036	0.66
6.00	0.00507	0.0507	0.628	0.86372	-0.2248	5	1.0	0.033	0.68
6.00	0.00507	0.0507	0.628	0.86372	-0.2248	5	1.0	0.025	0.64
6.00	0.00507	0.0507	0.628	0.86372	-0.2248	5	1.0	0.014	0.66
6.00	0.00184	0.0507	0.628	0.86372	-0.2248	5	1.0	0.0091	0.64
6.30	0.0074	0.037	0.440	0.874164	-0.1204	6	1.5	0.031	0.67
6.30	0.00363	0.0363	0.430	0.874164	-0.1152	6	1.5	0.0214	0.66
6.30	0.0012	0.0363	0.432	0.874164	-0.1162	6	1.5	0.0115	0.67
6.72	0.0048	0.024	0.286	0.885773	-0.0533	6	2.0	0.02	0.74
6.72	0.0024	0.024	0.286	0.885773	-0.0533	6	2.0	0.0167	0.76
6.72	0.00084	0.0231	0.274	0.885773	-0.0491	6	2.0	0.0125	n.a.

TABLE IV: Parameters of the HISQ ensembles with the strange and charm quark masses at or close to their physical values. The ensembles are listed in the same order as in Table I. The first column gives the gauge coupling constant $10/g^2$, and the second, third and fourth columns the masses of the light, strange and charm quarks in lattice units. The fifth column is the tadpole coefficient u_0 obtained from the fourth-root of the plaquette, and the sixth is the mass-dependent correction to the tree-level improvement of the charm quark dispersion relation, or Naik term, ϵ_N. (The two values of ϵ_N with stars use the bare mass, rather than the tree-level mass in Eq. (26) of Ref. [4], giving rise to a difference that appears at order am_c^6). s is the separation of stored configurations and len., the length of a trajectory, both in simulation time units. ϵ is the molecular dynamics step size, and acc. is the fraction of the trajectories accepted.

of simulations with the asqtad quark action [1], several of the largest ensembles were run with the RHMD algorithm in which the accept-reject step at the end of each trajectory is omitted. This is an attractive possibility because it allows running at a step size limited by its effects on physical quantities, and because the lattice generation can be done in single

am_{l1}	am_{l2}	am_s	am_c	ϵ	acc.
0.00507	0.00507	0.00507	0.628	0.02	0.67
0.00507	0.00507	0.012675	0.628	0.02	0.68
0.00507	0.00507	0.022815	0.628	0.02	0.70
0.00507	0.00507	0.0304	0.628	0.0227	0.68
0.01275	0.01275	0.01275	0.640	0.0278	0.71
0.0102	0.0102	0.03054	0.635	0.0294	0.74
0.0088725	0.0088725	0.022815	0.628	0.02	0.70
0.00507	0.012675	0.022815	0.628	0.02	0.73

TABLE V: Parameters of the HISQ ensemble with lighter-than-physical strange quarks. The ensembles are listed in the same order as in Table II, and the notation is the same as in Table IV, except that we distinguish between the masses of the two light quarks, because for the ensemble in the last row they are unequal. For all of these ensembles, $10/g^2 = 6.00$, $u_0 = 0.86372$, $\epsilon_N = -0.2248$, $s = 5$, and len.=1.0.

precision. (Double precision is necessary for the RHMC algorithm on large lattices because the numerical error in evaluating the action at the beginning and end of the trajectory in order to compute its change, ΔS, becomes of order one, making the accept/reject step nonsensical. The cost of double precision can be reduced by running the conjugate gradient in the molecular dynamics steps in single precision, followed by double precision refinement of the result.)

It is not possible to use the RHMD algorithm on coarse lattices because of the occurrence of spikes in the fermion force. For such lattices, if one uses the RHMD algorithm with the exact Hamiltonian in the molecular dynamics evolution of the gauge fields, then it is necessary to use a very small step size in order to perform the integration of the molecular dynamics equations accurately, whereas if one uses the guiding Hamiltonian, which ignores these spikes, there will be a significant deviation of the resulting gauge fields from the correct ones. However, as the lattice spacing decreases, the gauge fields become smoother, and spikes in the fermion force become less pronounced and very infrequent. This is fortunate, since it is the very challenging ensembles with small lattice spacings for which the RHMD algorithm would provide the greatest gain if applicable. We have tested the efficacy of the RHMD
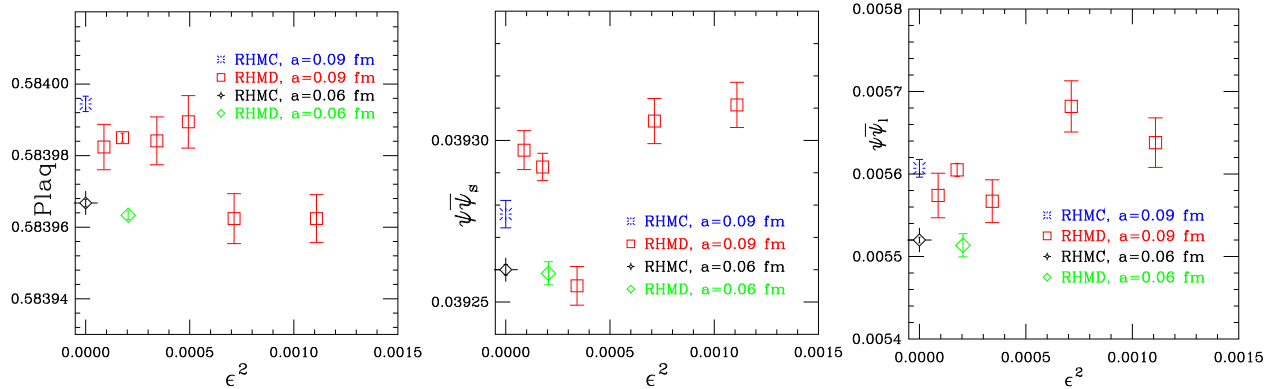
FIG. 1: Comparison of the RHMC and RHMD algorithms for the $a \approx 0.09$ fm, physical quark mass and $a \approx 0.06$ fm, $m_l = m_s/10$ ensembles. The RHMD points are plotted at the value of the molecular dynamics step size ϵ for which they were generated, and are given by red squares for the $a \approx 0.09$ fm ensemble, and by green diamonds for the $a \approx 0.06$ fm one. The RHMC points are plotted at $\epsilon = 0$, and are given by blue bursts for the $a \approx 0.09$ fm ensemble and by fancy black diamonds for the $a \approx 0.06$ fm one. The left panel shows the plaquette, the central panel the strange-quark $\langle \bar{\psi}\psi \rangle$, and the right panel the light-quark $\langle \bar{\psi}\psi \rangle$, all as a function of ϵ^2. A significant fraction of the total sample for $a \approx 0.09$ fm was run at $\epsilon^2 = 0.000177$, which is why the error bars at that point are so small. Both the light and strange quark $\langle \bar{\psi}\psi \rangle$ are given in lattice units, and both are calculated in double precision. The points for the $a \approx 0.06$ fm ensemble have been shifted vertically to move them into the range of the graph, the plaquette downward by 0.031643, the strange and light quark $\langle \bar{\psi}\psi \rangle$ upward by 0.0157497 and 0.00185230, respectively.

algorithm on two of our ensembles, those with lattice spacing $a \approx 0.09$ fm and physical light quark mass, and with lattice spacing $a \approx 0.06$ fm and $m_l = m_s/10$. For the first of these ensembles we have run a few RHMD trajectories at a number of different step sizes, and generated a significant fraction of our total sample with this algorithm at a step size of $\epsilon = 0.0133$, which compares with the step size of 0.0115 used in the RHMC part of the ensemble. Although the step size used in the RHMD sub-ensemble is only a little larger than that in the RHMC sub-ensemble, large gains are realized from running in single precision and from not rejecting up to one third of the trajectories.

We have compared several quantities computed separately on the RHMC and RHMD sub-ensembles. Results for the plaquette and the light- and strange-quark condensates $\langle \bar{\psi}\psi \rangle$ on the $a \approx 0.09$ fm physical quark mass ensemble are shown in Fig. 1. The plaquette

	RHMC	RHMD	difference
aM_π	0.05716(9)	0.05717(5)	0.00001(11)
$aM_{\bar{s}s}$	0.30608(14)	0.30624(10)	0.00016(17)
aM_{η_c}	1.32708(6)	1.32718(5)	0.00010(8)

TABLE VI: Pseudoscalar meson masses for the $a \approx 0.09$ fm physical quark mass RHMC and RHMD ($\epsilon = 0.0133$) sub-ensembles. The fit ranges and fit forms are not necessarily those that would be used for a final spectrum analysis, but care has been taken to use the same fit ranges in each sub-ensemble.

shows the expected effect proportional to ϵ^2, while the strange-quark condensate is less regular, and the light quark condensate has large errors. The points with small error bars at $\epsilon^2 = (0.0133)^2 \approx 0.000177$ (third point from the left) are the points where production running was done with the RHMD algorithm. To estimate the physical significance of these effects, we may suppose that the effect is largely a change in the lattice spacing,

$$\Delta a = \frac{\partial a}{\partial \text{Plaq}} \frac{\partial \text{Plaq}}{\partial \epsilon^2} \epsilon^2 \quad . \tag{1}$$

Using the difference of the plaquettes at $\epsilon = 0$ and $\epsilon = 0.0133$, and the differences in plaquettes among ensembles at $a \approx 0.12$, 0.09 and 0.06 fm, we find that this corresponds to a shift in the lattice spacing of about 1.4×10^{-5} fm, or a fractional shift of about 1.6×10^{-4}.

The black fancy diamonds and green diamonds in Fig. 1 show the plaquette and strange $\langle \bar{\psi}\psi \rangle$ for the $a \approx 0.06$ fm $m_l = m_s/10$ run at $\epsilon = 0$ (RHMC) and $\epsilon = 0.0143$ (RHMD), with an arbitrary constant added to put them in the range of this graph. Here the effects are somewhat smaller than in the $a \approx 0.09$ fm ensemble, likely because the gauge configurations are smoother at the smaller lattice spacing.

While the plaquette and $\langle \bar{\psi}\psi_s \rangle$ are determined accurately enough so that the step size effects are visible, it is much more interesting to see how physical quantities are affected by the step size errors. Unfortunately, the only such quantities that can be determined with the required precision are the pseudoscalar meson masses. Table VI shows masses for the light-light, strange-strange and charm-charm pseudoscalar mesons in the RHMC and RHMD sub-ensembles.

From these results, we see that the use of the RHMD algorithm introduces a small systematic error, in comparison to other uncertainties. For all but a few quantities, this

m_l/m_s	f_{p4s} (MeV)	M_{p4s} (MeV)	ratio
1/5	157.7(0.1)(0.8)	437.6(0.5)(2.0)	0.3604(5)(30)
1/10	155.5(0.2)(0.6)	435.1(0.3)(1.1)	0.3575(6)(18)
1/27	154.0(0.4)(0.6)	434.5(0.1)(0.6)	0.3544(10)(15)

TABLE VII: The decay constant f_{p4s}, the meson mass M_{p4s} and their ratio from the 2+1 flavor asqtad analysis. The numbers in parentheses are the statistical and systematic errors, in that order.

error is also smaller than the statistical error. Among our current projects, the only quantity for which we cannot use the RHMD results is the interaction measure in high temperature QCD, where a delicate subtraction of the plaquette and $\langle \bar{\psi}\psi \rangle$ between the hot and cold lattices is needed. With this one exception, we believe that it is safe to use the RHMD algorithm for $a \leq 0.09$ fm, although we did use RHMC for the $a \approx 0.09$ fm, $m_l = m_s/5$ and $m_s/10$ ensembles.

III. SETTING THE LATTICE SCALE

Since lattice computations produce quantities in units of the lattice spacing, converting to physical units, such as MeV or fm, requires accurate knowledge of the lattice spacing. This is done by computing some physical quantity which is experimentally well known and can be accurately computed on the lattice. Examples in common use include the Ω^- mass, the splittings of charmonium levels, and the pion or kaon decay constant. These quantities can be used to fix the lattice spacing in physical units, and thus to convert other measurements to physical units. In simulation programs with multiple ensembles, it is often convenient to use an intermediate interpolating quantity which is easily measured on the lattice, but may not be an experimentally accessible quantity, such as the commonly used Sommer scales r_0 and r_1 [20]. This interpolating quantity can be fixed by calculating a physical quantity on some of the ensembles, often with a fitting or smoothing procedure, or even from a completely different set of simulations.

Strictly speaking, observables measured on the lattice take on their physical values only in the continuum limit at physical valence- and sea-quark masses. Therefore, the definition of the lattice spacing for unphysical quark masses or non-zero lattice spacings is somewhat

arbitrary. The definition can be made by requiring that the interpolating quantity be independent of the lattice spacing and sea-quark masses, or by fixing its dependence on these quantities to some plausible ansatz, such as that predicted by chiral perturbation theory at some order. Of course, different ansätze are expected to give identical results only in the continuum, physical quark-mass limit.

Here we present determinations of the lattice scale on the HISQ ensembles from two such interpolating quantities, r_1 and f_{p4s}. The first of these is calculated from the static-quark potential, and was used extensively in our earlier simulation program using the asqtad action as described in Ref. [1]. The second quantity, f_{p4s}, is a variant of a method suggested in Ref. [21]. This is the decay constant of a pseudoscalar meson with valence-quark masses 0.4 times the strange-quark mass. Ultimately, we expect that our preferred scale-setting will be based on f_π. The scale setting via f_π will largely follow the same approach as described for f_{p4s} here, since f_π and f_{p4s} are determined from the same types of correlators and differ only in the quark masses. The value $0.4\,m_s$ was chosen to be heavy enough to allow relatively cheap determination on the lattice ensembles, but light enough that chiral perturbation theory can accurately describe its dependence on the valence- and sea-quark masses.

Since we do not know the correct valence strange-quark mass until after the lattice spacing is fixed, f_{p4s} and $0.4\,m_s$ must be determined self-consistently. Roughly speaking, this is done by finding the valence-quark mass am_q where af_{p4s} and aM_{p4s}, the mass of the pseudoscalar meson with valence quark mass $0.4\,m_s$, have their expected ratio, as we now explain.

For now, we use "physical" values of f_{p4s} and M_{p4s} determined from fits to pseudoscalar meson masses and amplitudes in the MILC 2+1 flavor asqtad action ensembles [1]. In practice, these come from evaluating the chiral-continuum extrapolation fit function for the pseudoscalar meson mass and decay constant at the appropriate bare-quark masses: strange sea-quark $m_s = m_s^{\text{physical}}$, light-to-strange sea-quark mass ratio m_l/m_s equal to the simulated value for that ensemble, and degenerate valence-quark masses $m_{\text{valence}} = 0.4\,m_s^{\text{physical}}$.

These values are shown in Table VII. Clearly, when a similar analysis of the HISQ pseudoscalar mesons is available, f_{p4s} and m_{p4s} from that analysis will be used instead.

The determination of af_{p4s} on one ensemble begins with calculating pseudoscalar meson masses and decay constants for several valence-quark masses. In our ensembles, the valence-quark masses used include $0.3\,m_s'$, $0.4\,m_s'$ and $0.6\,m_s'$, where m_s' is the strange-quark mass estimated before the ensemble was started, which in most cases is the same as the strange

$10/g^2$	am_l	am_s	am_c	r_1/a	af_{p4s}	am_{p4s}
5.80	0.013	0.065	0.838	2.059(23)	0.12150(18)	0.02744(9)
5.80	0.0064	0.064	0.828	2.073(13)	0.12042(11)	0.02744(5)
5.80	0.00235	0.0647	0.831	2.089(8)	0.11948(6)	0.02762(3)
6.00	0.0102	0.0509	0.635	2.575(17)	0.09780(12)	0.02139(6)
6.00	0.00507	0.0507	0.628	2.585(19)	0.09614(14)	0.02111(7)
6.00	0.00507	0.0507	0.628	2.626(13)	0.09613(9)	0.02118(5)
6.00	0.00507	0.0507	0.628	2.614(9)	0.09605(7)	0.02113(4)
6.00	0.00184	0.0507	0.628	2.608(8)	0.09530(5)	0.02130(2)
6.30	0.0074	0.037	0.440	3.499(24)	0.07093(11)	0.01482(5)
6.30	0.00363	0.0363	0.430	3.566(14)	0.06953(6)	0.01467(3)
6.30	0.0012	0.0363	0.432	3.565(13)	0.06865(4)	0.01462(2)
6.72	0.0048	0.024	0.286	5.342(16)	0.04660(7)	0.00918(3)
6.72	0.0024	0.024	0.286	5.376(14)	0.04545(5)	0.00896(2)

TABLE VIII: r_1/a, af_{p4s} and am_{p4s}, measured on the ensembles with physical strange- and charm-quark masses. These quantities are used to determine the lattice spacing, which is given in the next table. (Note that m_{p4s} is the quark mass corresponding to f_{p4s}.)

sea-quark mass used in generating the ensemble. We then interpolate the square $(M_{p4s}/f_{p4s})^2$ as a quadratic function of the bare valence-quark mass. We use $(M_{p4s}/f_{p4s})^2$ rather than alternatives, such as f_{p4s}/M_{p4s}, since we expect M_{p4s}^2 to be approximately linear in am_q, and f_{p4s} to be approximately constant. The valence-quark mass at which $(M_{p4s}/f_{p4s})^2$ has the desired value is then the physical $0.4\,m_s$. The decay constant in lattice units af_{p4s} is then found by similarly interpolating $(af_{p4s})^2$ as a quadratic function of the bare quark masses and evaluating it at $0.4\,m_s$. Next, the lattice spacing is obtained by requiring that f_{p4s} on this ensemble equals the desired value. Finally, M_{p4s} is found from f_{p4s} and the ratio. Errors on this quantity are found by a jackknife analysis, where blocks of 16 lattices are omitted from the completed ensembles, and blocks of 8 lattices from the ensembles that are approximately 50% completed. The resulting values for af_{p4s}, am_{p4s} and the lattice spacing in fermi are shown in Tables VIII, IX, and X. In these tables, the error in a_{r_1} $(a_{f_{p4s}})$ (fm) includes the statistical and systematic errors in the physical value of r_1 (f_{p4s}), combined in

$10/g^2$	am_l	am_s	am_c	a_{r_1} (fm)	$a_{f_{p4s}}$ (fm)	$am_s^{r_1,tuned}$	$am_s^{f_{p4s},tuned}$	$am_c^{r_1,tuned}$	$am_c^{f_{p4s},tuned}$
5.80	0.013	0.065	0.838	0.1510(20)	0.1520(8)	0.0668(15)	0.0678(3)	0.8472(16)	0.8514(16)
5.80	0.0064	0.064	0.828	0.1499(14)	0.1528(6)	0.0671(3)	0.0686(1)	0.8407(7)	0.8489(7)
5.80	0.00235	0.0647	0.831	0.1488(11)	0.1531(7)	0.0655(5)	0.0690(1)	0.8351(9)	0.8522(9)
6.00	0.0102	0.0509	0.635	0.1207(11)	0.1224(6)	0.0516(7)	0.0535(2)	0.6363(9)	0.6489(10)
6.00	0.00507	0.0507	0.628	0.1202(12)	0.1220(5)	0.0514(7)	0.0528(2)	0.6310(10)	0.6375(10)
6.00	0.00507	0.0507	0.628	0.1184(10)	0.1220(5)	0.0500(5)	0.0530(1)	0.6241(8)	0.6376(8)
6.00	0.00507	0.0507	0.628	0.1189(9)	0.1219(5)	0.0504(4)	0.0528(1)	0.6263(7)	0.6372(7)
6.00	0.00184	0.0507	0.628	0.1191(7)	0.1221(6)	0.0507(3)	0.0533(1)	0.6271(10)	0.6378(10)
6.30	0.0074	0.037	0.440	0.0888(8)	0.0887(5)	0.0367(5)	0.0370(2)	0.4396(7)	0.4393(7)
6.30	0.00363	0.0363	0.430	0.0872(7)	0.0882(4)	0.0358(3)	0.0367(1)	0.4288(5)	0.4325(5)
6.30	0.0012	0.0363	0.432	0.0871(6)	0.0880(4)	0.0357(3)	0.0365(1)	0.4294(5)	0.4323(5)
6.72	0.0048	0.024	0.286	0.0582(4)	0.0583(3)	0.0225(1)	0.0230(1)	0.2768(3)	0.2772(3)
6.72	0.0024	0.024	0.286	0.0578(4)	0.0577(2)	0.0224(1)	0.0224(1)	0.2750(2)	0.2755(3)

TABLE IX: Lattice spacing and the retuned strange- and charm-quark masses, set by using r_1 and f_{p4s} quantities for ensembles with physical strange-and charm-quark masses. For the $am_l = 0.00184$ ensemble the J/Ψ mass is not available, so the η_c mass was used in tuning instead.

quadrature with the statistical error in r_1/a (af_{p4s}). For the physical value of r_1 we use $r_1 = 0.3106(8)(14)(4)$, obtained from an analysis of pseudoscalar decay constants on lattices generated with the asqtad quark action [26]. Errors in the physical lattice spacings in these tables combine the errors in the physical value of r_1 with the statistical errors in r_1/a. Again, we will eventually determine the physical r_1 with the HISQ ensembles. Because r_1 is not experimentally observable, however, we will still need to use a measured quantity such as f_π or the Υ 1S-2S mass splitting to obtain r_1 in physical units.

To find the tuned charm-quark mass, we calculated pseudoscalar and vector charmonium masses for two valence-quark masses: the sea charm-quark mass and 0.9 times the sea charm-quark mass. Using linear interpolation, we find the valence charm quark mass where the spin-averaged charmonium mass has its physical value. Of course, this depends on the previous determination of the lattice spacing, so we quote two values, where the lattice spacing was determined from r_1 or from f_{p4s}.

am_{l1}	am_{l2}	am_s	am_c	r_1/a	af_{p4s}	am_{p4s}	a_{r_1} (fm)	$a_{f_{p4s}}$ (fm)
0.00507	0.00507	0.00507	0.628	2.675(16)	0.08973(9)	0.01900(5)	0.1161(10)	0.1139(10)
0.00507	0.00507	0.012675	0.628	2.676(16)	0.09109(9)	0.01944(4)	0.1161(9)	0.1156(5)
0.00507	0.00507	0.022815	0.628	2.653(13)	0.08973(10)	0.01903(4)	0.1171(8)	0.1139(5)
0.00507	0.00507	0.0304	0.628	2.647(15)	0.09383(8)	0.02042(4)	0.1173(9)	0.1191(5)
0.01275	0.01275	0.01275	0.640	2.642(21)	0.09391(14)	0.02038(6)	0.1176(11)	0.1192(5)
0.0102	0.0102	0.03054	0.635	2.593(19)	0.09569(15)	0.02099(6)	0.1198(11)	0.1214(5)
0.0088725	0.0088725	0.022815	0.628	2.646(16)	0.09416(12)	0.02055(4)	0.1174(9)	0.1195(5)
0.00507	0.012675	0.022815	0.628	2.664(16)	—	—	0.1166(9)	—

TABLE X: r_1/a, af_{p4s} and am_{p4s} for the ensembles with unphysical strange-quark mass. The lattice spacings determined from these quantities are given in the last two columns. Since the purpose of these lattices is to study dependence as the quark masses are varied, and because we do not know the dependence of the physical f_{p4s} on the strange quark mass, the value appropriate for $m_l = m_s/10$, 155.5(2)(6) MeV, is used for all of these ensembles. (As in Table VIII, m_{4ps} is the quark mass corresponding to f_{4ps}).

In Table IX we compare lattice spacings and retuned strange- and charm-quark masses based on the r_1 and f_{p4s} scales. In general, we observe good agreement in the lattice spacing and the strange-quark mass, with the largest difference in the latter of about 5-6% for some of the $a \approx 0.12$ and 0.15 fm ensembles. As expected, the difference in the lattice spacing and retuned quark masses decreases towards the continuum and is small on the finest, $a \approx 0.06$ fm ensembles.

IV. TOPOLOGICAL SUSCEPTIBILITY

The topological susceptibility

$$\chi_t = \langle \nu^2 \rangle / V \qquad (2)$$

measures fluctuations in the total topological charge ν in the space-time volume V. The angle brackets represent an average over the gauge-field configurations. These fluctuations are suppressed at small quark mass. Leading-order continuum chiral perturbation theory predicts [27] that

≈ a (fm)	m_l/m_s	$M_{\pi,I}^2 r_0^2$	$\chi_t r_0^4$
0.12	1/5	1.006	0.0170(5)
0.12	1/27	0.560	0.0108 (2)
0.09	1/5	0.736	0.0124 (7)
0.09	1/27	0.282	0.0059 (4)
0.06	1/5	0.603	0.0075 (8)

TABLE XI: Topological susceptibility for the indicated HISQ ensembles *vs.* taste-singlet pion mass squared in units of r_0.

$$\chi_t V \approx x \equiv V\Sigma m', \tag{3}$$

where Σ is the chiral condensate parameter and m' is the reduced mass of the quarks:

$$1/m' = 1/m_u + 1/m_d + 1/m_s + \dots . \tag{4}$$

The relation (3) is valid provided $x \gg 1$, which is the case for our simulations.

For equal up- and down-quark masses we may use the Gell-Mann-Oakes-Renner relation, also from leading-order chiral perturbation theory, to rewrite this expression as

$$f_\pi^2/(4\chi_t) = 2/M_{\pi,I}^2 + 1/M_{ss,I}^2 + \dots, \tag{5}$$

where $M_{ss,I}^2 = 2M_{K,I}^2 - M_{\pi,I}^2$ is the squared mass of the fictitious pseudoscalar meson containing two nonannihilating quarks with masses equal to the strange quark. In our normalization the pion decay constant f_π is approximately 130 MeV. In leading order *staggered* chiral perturbation theory, the meson masses appearing in Eq. (5) are taste-singlet masses, as indicated by the subscript I.

Confirming Eq. (3) provides an essential test of the fourth-root treatment of the fermion determinant, since it gives a nearly direct measure of the influence of sea quarks on the gauge field. Since the right-hand side depends on the taste-singlet mass splitting, it also tests the degree of improvement of the staggered action.

In Ref. [28] we presented results for the topological susceptibility over a wide range of light-quark masses and lattice spacings with $2 + 1$ flavors of improved (asqtad) quarks. Here, we use the same methods to determine the topological susceptibility in the presence

FIG. 2: The time history of the topological charge for five HISQ gauge configuration ensembles. The histogram to the right of each time history shows the distribution of charges.

of $2+1+1$ flavors of HISQ sea quarks and compare results with the asqtad study. We have studied five of the HISQ ensembles, namely three with $m_l = m_s/5$ and $a \approx 0.06$, 0.09, and 0.12 fm, and two at the physical Goldstone pion mass with $m_l \approx m_s/27$ and $a \approx 0.09$ and 0.12 fm.

In brief, we use the Boulder discretization [29, 30] of the topological charge density

$$\rho(x) = \frac{1}{32\pi^2} F_{\mu\nu}^a \widetilde{F}_{\mu\nu}^a, \tag{6}$$

measured after three HYP smoothing sweeps [31] of the gauge field. The topological susceptibility is then obtained from density-density correlations:

$$\chi_t = \int d^4x\, C(r) \quad \text{with} \quad C(r) = \langle \rho(x)\rho(0) \rangle , \tag{7}$$

Although in the continuum limit this definition suffers from ultraviolet singularities that require regularization [32], such complications are unimportant at our range of lattice spacings [28].

As in Ref. [28], we reduce the variance in the integral in Eq. (7) by fitting $C(r)$ at large r to a model that includes the required contributions from the η and η' mesons. The relative strength of the two contributions is also fixed using tree-level chiral perturbative mixing. The integral is then evaluated as

$$\chi_t = \int_{r<r_{\text{cut}}} d^4x \, C(r) + \int_{r>r_{\text{cut}}} d^4x \, C(r) \,, \tag{8}$$

where the contribution for $r > r_{\text{cut}}$ is derived from the asymptotic fit and for $r < r_{\text{cut}}$ it is based on the raw data. In practice, we take $r_{\text{cut}} \approx 1.2$ fm.

An interesting question for any lattice QCD simulation is whether the tunneling rate between topological charge sectors is sufficient to bring those sectors to equilibrium. To investigate this question, we show in Fig. 2 the time history of the topological charge for five HISQ ensembles: those with $m_l = m_s/5$ and $a \approx 0.12$, 0.09 and 0.06 fm, and with $m_l = m_s/27 \approx 0.037 \, m_s$ for $a \approx 0.12$ and 0.09 fm. (We do not yet have sufficient data to make a similar plot for the $a \approx 0.06$ fm, physical quark-mass ensemble). To the right of each time history plot, we show a histogram of the topological charge. As expected, the tunneling rate decreases with the lattice spacing, whereas the fluctuations of the charge increase as the light quark mass is decreased. It is clear from this figure that the simulation is exploring a wide range of topological charges. The topological susceptibility determined from the widths of these histograms is consistent with the results in Table XI, although with larger statistical errors.

Results are tabulated in Table XI and compared with those for asqtad in Fig. 3. The comparison with the asqtad results provides a clear demonstration of the improvement in the HISQ configurations. Because the susceptibility is computed without involving valence quarks, this comparison directly tests whether the change in sea quark action leads to the expected improvement in the gauge configurations. We observe in Fig. 3 that the HISQ points with $a \approx 0.12$, 0.09 and 0.06 fm are near the asqtad curves with $a \approx 0.09$, 0.06 and 0.045 fm, respectively. The HISQ points are to the left of the corresponding asqtad points because the horizontal axis is the mass of the taste singlet pion (the heaviest pion taste), and the reduction in taste symmetry breaking moves the HISQ points to the left. It is the decrease of the susceptibility for the HISQ configurations relative to those of the asqtad configurations that represents the improvement in the gauge configurations.
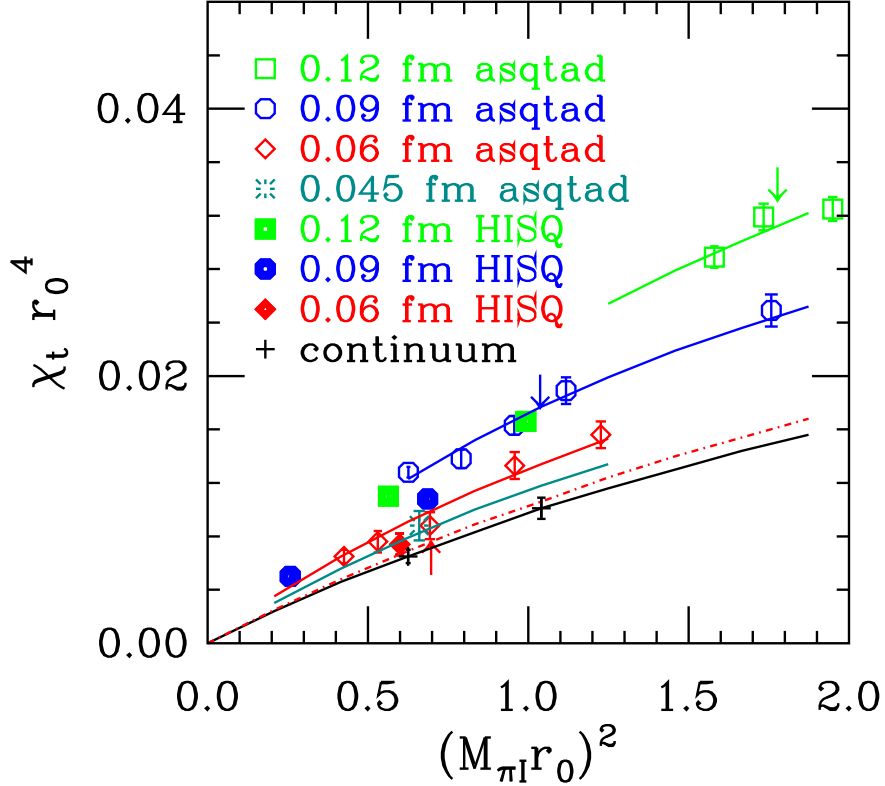
FIG. 3: Topological susceptibility *vs.* taste-singlet pion mass squared in units of r_0, comparing results from five HISQ ensembles (filled symbols) with previously published asqtad results [28] (open symbols). Solid curves are from a joint chiral/continuum fit to the asqtad data for the four lattice spacings shown in the figure. The lowest (black) curve indicates the resulting continuum extrapolation of the asqtad fit with two representative points displaying the extrapolation errors. The (red) dot-dashed curve shows the leading order prediction in chiral perturbation theory. The (green) arrow above the (green) 0.12 fm asqtad curve indicates the asqtad point with a light quark mass comparable to that of the upper solid (green) HISQ square. Similarly, the (blue) arrow above the (blue) 0.09 fm asqtad curve indicates the asqtad point with a light quark mass comparable to the upper solid (blue) HISQ octagon, and the (red) arrow below the (red) 0.06 fm asqtad curve locates the asqtad point with a light quark mass comparable to the solid (red) HISQ diamond.

V. TASTE SYMMETRY

For the $m_l = m_s/5$ ensembles at each lattice spacing, we have measured the masses of pseudoscalar mesons of all 16 possible tastes: I, ξ_μ, $\xi_{\mu\nu}$, $\xi_{\mu5}$, and ξ_5, with $\xi_{\mu\nu} \equiv [\xi_\mu, \xi_\nu]/2$ and $\xi_{\mu5} \equiv \xi_\mu \xi_5$. Figure 4 shows the difference in squared mass between pions of a given taste

and that of the Goldstone pion (taste ξ_5), plotted versus $\alpha_S^2 a^2$, the expected dependence of the leading taste-violating effects. The splittings for the corresponding asqtad ensembles are also shown for comparison. Here "pion" means the unitary meson with degenerate valence masses equal to m_l. Tastes are labeled by their index or indices; *i.e.*, ij denotes taste ξ_{ij}, with i and j labeling generic spatial directions. Results for different spatial taste indices have been averaged since exact (discrete) lattice symmetries imply that their masses are equal. In most cases, the differences between squared masses have been calculated with a jackknife procedure.

One can see that the HISQ splittings are typically a factor of three smaller than the asqtad ones at the same lattice spacing. In fact the improvement with HISQ increases as the lattice spacing decreases, so that at $a \approx 0.06$ fm, the HISQ splittings are a factor of 6 to 8 smaller than the asqtad ones. Indeed the HISQ splittings at a given lattice spacing are comparable to, but somewhat smaller than, the asqtad splittings at the next smaller lattice spacing, *i.e.*, HISQ splitting at $a \approx 0.09$ fm are a bit smaller than asqtad splittings at $a \approx 0.06$ fm.

For the strong coupling α_S, we use α_V, the coupling from the asqtad heavy-quark potential, calculated in Ref. [33] at next-to-leading order in tadpole-improved lattice perturbation theory [34]:

$$ -\ln(\mathrm{plaq}) = 3.0682(2)\,\alpha_V(3.33/a)\left[1 + \alpha_V\{-0.770(4) - 0.09681(9)\,n_f\}\right], \qquad (9) $$

where plaq is the average plaquette of the ensemble, n_f is the number of sea-quark flavors, and the scale $q^* = 3.33/a$ for the plaquette is set by the BLM procedure [35]. For taste-violations with asqtad quarks, one expects the appropriate scale to be somewhat lower, since the asqtad smearings are designed to remove coupling of the quarks to gluons with any momentum component equal to π/a. In Fig. 4, we choose scale $q^* = 2/a$ for α_V (the adjustment of scale is made using the universal two-loop formula). For the HISQ action, the perturbative calculation corresponding to Eq. (9) has not to our knowledge been performed. However, since the dependence on n_f in Eq. (9) is fairly small, we think it is reasonable also to use the asqtad formula for HISQ, at least in this qualitative comparison of discretization effects. One can see that the HISQ points are shifted to the right relative to corresponding asqtad ones; this is the effect of using $n_f = 4$ rather than $n_f = 3$.

By comparing the asqtad splittings in Fig. 4 with the upper line (which has slope 1),
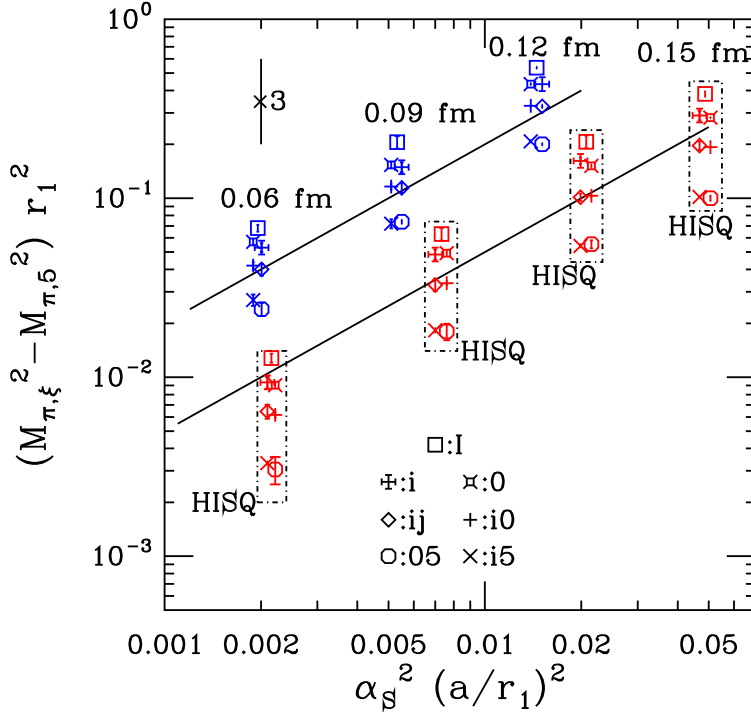
FIG. 4: Pion taste splitting of pions for asqtad (blue) and HISQ (red) actions. For clarity, the HISQ splittings are also enclosed in dashed-dotted boxes, and nearly degenerate masses have been displaced slightly in the horizontal direction. Differences between the squared masses of various taste pions and that of the Goldstone pion are shown in units of r_1, and plotted versus the expected leading dependence of taste violations in the theory, $\alpha_S^2 a^2$, also in r_1 units. Here, we use $\alpha_S = \alpha_V$ at scale $q^* = 2/a$. The two diagonal lines are not fits, but merely lines with slope 1, showing the expectation if the splittings are linear in $\alpha_S^2 a^2$. The vertical line at the upper left shows the displacement associated with a factor of three in splittings. The numerical values of the HISQ taste splittings plotted here are given in Table XIV of the appendix.

one can see that the asqtad splittings are almost proportional to $\alpha_V^2(2/a)\, a^2$, but fall very slightly faster as a decreases. The HISQ splittings fall still more rapidly at the smallest lattice spacings, presumably because the proper choice of q^* is significantly smaller in the HISQ case. That is reasonable, since the greater smearing present in the HISQ action should produce greater damping of the couplings of gluons to quarks at high momenta. On the other hand, the HISQ splittings fall more slowly than $\alpha_V^2(2/a)\, a^2$ at the coarsest lattice spacings (between 0.15 fm and 0.12 fm), which is evidence for higher order ($\alpha_S^3 a^2$ or a^4) contributions.
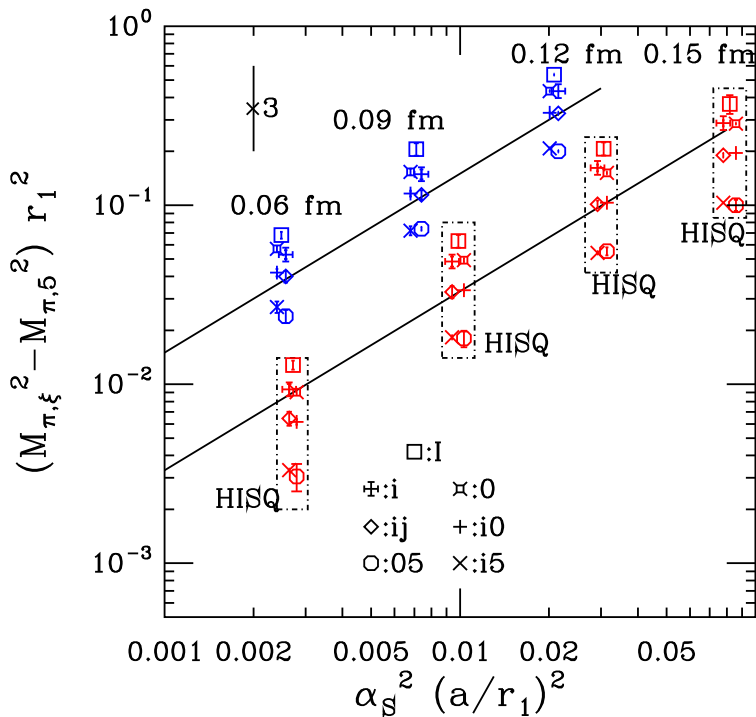
FIG. 5: Same as Fig. 4, but with $\alpha_S = \alpha_V(q^* = 1.5/a)$.

For comparison, Fig. 5 shows the effect of choosing a somewhat lower scale, $q^* = 1.5/a$, in other words $\alpha_S = \alpha_V(1.5/a)$. Now the asqtad splittings fall slightly slower than $\alpha_S^2 a^2$ as a decreases, while the HISQ splittings are closer to linear, but still fall faster between 0.09 fm and 0.06 fm. We could continue to reduce q^* until this drop became linear, but it would be an arbitrary exercise since we do not have the correct perturbative formula in the HISQ case.

In Figs. 4 and 5, both the HISQ and asqtad masses show an approximate $SO(4)$ taste symmetry: The masses form five multiplets with tastes P, A, T, V, and I (pseudoscalar, axial-vector, tensor, vector and singlet tastes). This is an "accidental" symmetry, because the exact lattice symmetries do not require this structure, but would allow all eight multiplets listed in the legends to be non-degenerate. The origin of the $SO(4)$ taste symmetry of pions [36] is explained briefly below.

The $SO(4)$ symmetry is seen even more clearly in the $\bar{l}l$ (pion) masses in Fig. 6. Up to quite small errors, no breaking of the symmetry is visible. The $\bar{l}l$ masses also obey a rough "equal spacing rule" of squared masses between the P, A, T, V, and I tastes (and with that ordering). The equal spacing is familiar from the asqtad case [1]. It arises in staggered chiral

perturbation theory (SχPT) [36, 37] from the fact that the dominant taste-breaking chiral operator (*i.e.*, the one with the largest coefficient) is

$$\mathcal{O}_4 = a^2 \text{Tr}(\xi_{\lambda 5} \Sigma \, \xi_{5\lambda} \Sigma) + h.c. \tag{10}$$

where *h.c.* stands for the Hermitian conjugate, and $\Sigma = \exp(i\Phi/f)$, with Φ the pion field and f the LO pion decay constant.

Operators such as $\mathcal{O}_4$ are representatives, at the chiral level, of taste-symmetry-breaking four-quark operators in the Symanzik effective theory. The four-quark operators may be labeled by the spin and taste of the bilinears from which they are constructed. In particular, $\mathcal{O}_4$ is generated by the operators $[I \times A]$, $[T \times A]$ and $[P \times A]$, where, for example

$$[T \times A] \equiv a^2 \left(\bar{q}\,\gamma_{\mu\nu} \otimes \xi_{\lambda 5}\, q\right) \left(\bar{q}\,\gamma_{\nu\mu} \otimes \xi_{5\lambda}\, q\right) , \tag{11}$$

with $\gamma_{\mu\nu} \equiv [\gamma_\mu, \gamma_\nu]/2$. This notation is basically that of Lee and Sharpe [36], except that we use I instead of S to denote scalar spin or taste, to avoid confusion with s for "strange." The four-quark operators that give rise to $\mathcal{O}_4$ are what are known as "type-A" operators, which are invariant under $SO(4)$ of taste, as well as the $SO(4)$ of Euclidean space-time rotations. There are also "type-B" operators that couple spin and taste indices, and break these $SO(4)$ symmetries down to a diagonal subgroup of joint spin-taste 90° rotations. An example is

$$[T_\mu \times A_\mu] \equiv a^2 \sum_{\mu=1}^{4} \left(\bar{q}\,\gamma_{\mu\nu} \otimes \xi_{\mu 5}\, q\right) \left(\bar{q}\,\gamma_{\nu\mu} \otimes \xi_{5\mu}\, q\right) . \tag{12}$$

The accidental $SO(4)$ taste symmetry of the pions results from the fact that the type-B operators do not have chiral representatives at LO. The non-trivial space-time structure in the type-B case requires more than two derivatives in the chiral operators, making their representatives next-to-leading order (NLO) in the chiral expansion [36].

Moving up in meson mass in Fig. 6, one sees that $SO(4)$ is still a good symmetry for the $\bar{l}s$ (kaon) and $\bar{s}s$ states, although some small symmetry violations are coming into view in the $\bar{s}s$ case. The $SO(4)$ violations for $\bar{s}s$ can be seen most clearly in Table XIV, where they are significant (though still quite small) at $a \approx 0.15$ fm. This is reasonable, since, as both the mass and lattice spacing increase, NLO chiral corrections are less suppressed, and these can violate $SO(4)$.

At still higher mass, ordinary light-meson SχPT ceases to be applicable, and a heavy-light version is necessary. For the case here, where both light and heavy quarks have the staggered
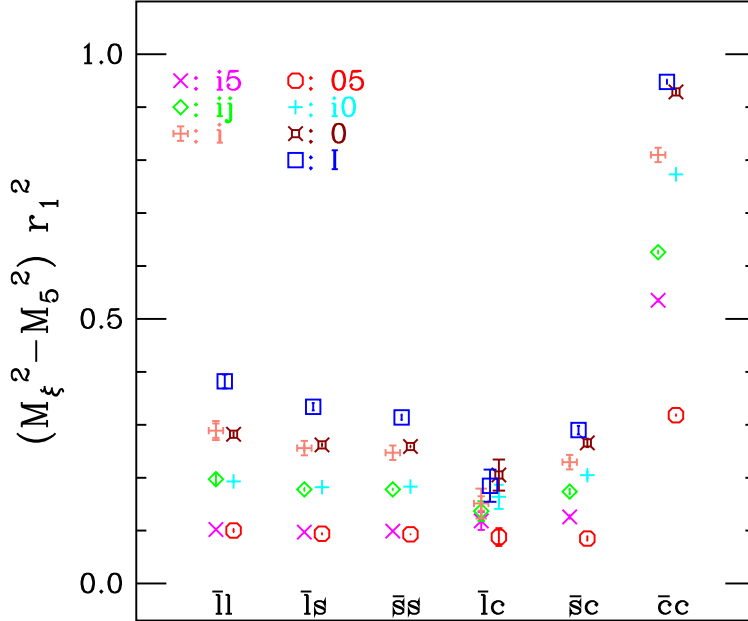
FIG. 6: Meson taste splittings on the $a \approx 0.15$ fm, $m_l = m_s/5$ ensemble. As in Fig. 4, the squared mass splitting between pseudoscalar mesons of different tastes and the lightest one with taste ξ_5 (the Goldstone pion for the $\bar{l}l$ case) is given in units of r_1. The types of quarks in the mesons are shown on the abscissa: l, s, and c stand for light (u, d), strange, and charm quarks, respectively. All mesons are the unitary ones, with each valence quark mass equal to one of the sea quark masses. Note, however, that all mesons here are treated as flavor-charged, so that even in the $\bar{s}s$ and $\bar{c}c$ cases, no quark-disconnected diagrams are included. The numerical values of most of these taste splittings are given in Tables XIV and XV of the appendix.

action, the heavy-light chiral theory has recently been worked out [38]. In that theory ("all-staggered heavy meson chiral perturbation theory" – ASHMχPT), the LO heavy-light chiral Lagrangian is of order k, the heavy-light meson residual momentum, which is taken to be of the order of the pion momentum $p \sim M_\pi$. This is different from the light-light case, in which the LO Lagrangian is order M_π^2. Taste violations are LO in the light-light case because the taste splittings in squared masses can be comparable to M_π^2; in other words we assume $a^2 \sim M_\pi^2$ (with appropriate factors of Λ_{QCD} inserted to make the dimensions the same). In the heavy-light case, on the other hand, taste violations are NLO since $a^2 \ll M_\pi^2$. This rough picture is actually consistent with what is seen in Fig. 6, where the splittings in squared masses remain comparable from the $\bar{l}l$ case through the $\bar{s}c$ case, and in Tab. XV, where we show the splittings in the $\bar{l}c$ and $\bar{s}c$ systems for the $a \approx 0.15$ fm, $m_l = m_s/5$ ensemble. The

splittings in the masses themselves are thus much smaller for $\bar{l}c$ or $\bar{s}c$ mesons than they are for $\bar{l}l$ mesons. For example, the measured taste splitting between the root-mean-squared (RMS) D_s meson and the lightest (taste ξ_5) D_s meson at $a \approx 0.12$ fm is only about 10 MeV, while it is about 110 MeV when the taste ξ_5 pion takes its physical mass. Fortunately, it is possible to show in ASHMχPT that the one-loop diagrams give taste-invariant masses to the heavy-light mesons, even though the diagrams contain pion propagators that break taste symmetry. This means that all taste-violations in the heavy-light masses at NLO come from analytic terms in the ASHMχPT Lagrangian, and may be analyzed straightforwardly.

There are other key differences between the light-light and heavy-light chiral theories. The non-relativistic nature of the heavy quark in heavy-light systems breaks space-time $SO(4)$ invariance and thereby introduces the four-velocity v^μ of the heavy quark explicitly into the heavy-light chiral theory. Factors of v^μ can substitute for derivatives in the chiral Lagrangian, and thereby allow type-B operators to have chiral representatives that are the same order in the chiral expansion as those from type-A operators. In addition, heavy-quark spin symmetry, which produces (approximate) degeneracy of the pseudoscalar (*e.g.*, D) and vector (*e.g.*, D^*) mesons, introduces spin degrees of freedom into the chiral theory. The gamma matrix γ_μ can then play a role similar to that of v^μ, also allowing type-B chiral operators to appear at the same order as type-A operators. The presence of type-B operators is visible in the breaking of $SO(4)$ symmetry for the heavy-light $\bar{l}c$ and $\bar{s}c$ mesons in Fig. 6. The splittings within $SO(4)$ multiplets are particularly clear in the $\bar{s}c$ case, where the statistical errors are smaller.

One can go further and study the particular pattern of taste splittings (both $SO(4)$ invariant and $SO(4)$ breaking) for heavy-light mesons. For this discussion, we assume that the lattice is sufficiently fine, or the charmed quark is sufficiently improved, that it may be treated as a "continuum-like," and corrections of order $(am_c)^2$ may be neglected. This means that the contributions of the heavy quark to the Symanzik effective theory are identical to those of a light quark. In particular, the same four-quark operators that dominated for light quarks, namely $[I \times A]$, $[T \times A]$ and $[P \times A]$, will be the dominant type-A operators in the heavy-light case. Taste splittings of heavy-light meson masses can come only from the "heavy-light" versions of these operators, $[I \times A]_{hl}$, $[T \times A]_{hl}$ and $[P \times A]_{hl}$, which couple

27

heavy and light bilinears, *e.g.,*

$$[T \times A]_{hl} \equiv a^2 \left(\bar{Q}\,\gamma_{\mu\nu} \otimes \xi_{\lambda 5}\,Q\right) \left(\bar{q}\,\gamma_{\nu\mu} \otimes \xi_{5\lambda}\,q\right) , \qquad (13)$$

where Q and q are the heavy- and light-quark fields, respectively.

In ASHMχPT, we define the heavy-light meson field H_j by[1]

$$H_j = \frac{1 + \not{v}}{2} \left[\gamma_\mu D^*_{\mu j} + i\gamma_5 D_j\right] , \qquad (14)$$

where j labels the light flavor, D_j and $D^*_{\mu j}$ are fields that annihilate pseudoscalar and vector mesons, respectively, and H_j, D_j and $D^*_{\mu j}$ are all 4×4 matrices in taste space. Then the four-quark operators above have the following chiral representatives:

$$\begin{aligned}
\left[I \times A\right]_{hl} &\rightarrow a^2 \mathrm{Tr}\left(\overline{H}\xi_{\lambda 5}H\xi_{5\lambda}\right) , \\
\left[P \times A\right]_{hl} &\rightarrow 0 , \\
\left[T \times A\right]_{hl} &\rightarrow a^2 \mathrm{Tr}\left(\overline{H}\gamma_{\mu\nu}\xi_{\lambda 5}H\gamma_{\nu\mu}\xi_{5\lambda}\right) ,
\end{aligned} \qquad (15)$$

where Tr is the trace over Dirac, taste, and flavor indices. Here we have set the pion field Φ to zero since we are not interested in couplings to pions, and have omitted two-trace terms, which vanish in that limit. The operator $[P \times A]_{hl}$ has no chiral representative in the heavy-light case because $(1 + \not{v})\gamma_5(1 + \not{v}) = 0$. (Only "upper components" of the heavy-quark field appear, while γ_5 couples upper and lower components.) Performing the traces in Eq. (15), the chiral operators give the relative contributions to the heavy-light pseudoscalar masses shown in Table XII. (The contributions from the two operators are proportional to each other because $\gamma_{\mu\nu}$ in Eq. (15) commutes with γ_5 from Eq. (14).) Note that the same equal-spacing rule and P, A, T, V, I ordering that appeared for light-light mesons also appears in the heavy-light case. This overall pattern is evident in the heavy-light lattice data in Fig. 6, although of course the taste-$SO(4)$ breaking produces additional structure.

For type-B operators, we have no experience from the light-light case as to which one or ones might give the largest contributions. However, we can guess that the four-quark operator $[T_\mu \times A_\mu]_{hl}$ would be dominant, since it is the only type-B operator that has the same spin and taste as one of the dominant type-A operators. The chiral operator generated

---

[1] For ease of comparison with the light-light case, we discuss the heavy-light chiral theory in Euclidean space, in contrast to what was done in Ref. [38].
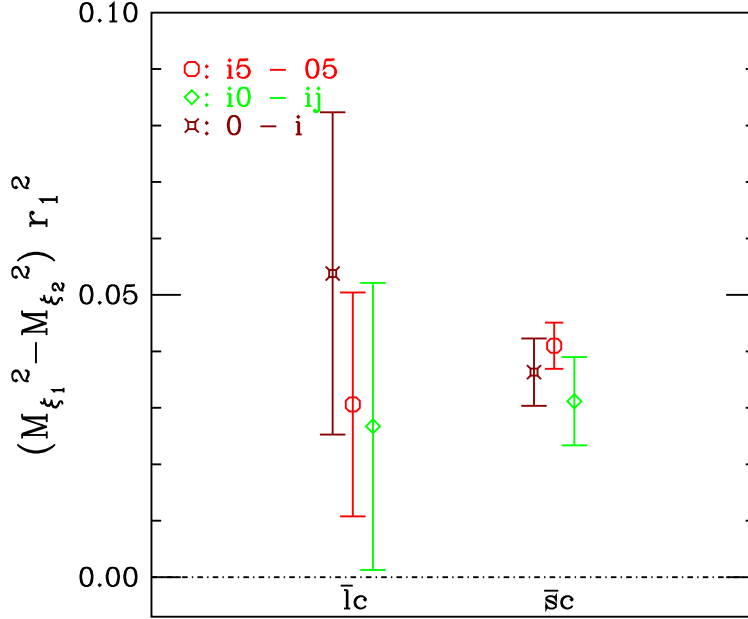
FIG. 7: Heavy-light taste splittings that break $SO(4)$ taste symmetry on the $a \approx 0.15$ fm, $m_l = m_s/5$ ensemble. As in Fig. 6, $\bar{l}c$ is a light-charm meson, and $\bar{s}c$ is a strange-charm meson. The errors in the squared-mass differences have been calculated with a jackknife procedure. The numerical values of these splittings are given in Table XV.

TABLE XII: Relative contributions to the masses of heavy-light mesons of given tastes due to the (apparently) dominant type-A operators, Eq. (15).

ξ_5	$\xi_{5\mu}$	$\xi_{\mu\nu}$	ξ_μ	I
-4	-2	0	+2	+4

is

$$\left[T_\mu \times A_\mu\right]_{hl} \to a^2 \sum_\mu \mathrm{Tr}\left(\overline{H}\gamma_{\nu\mu}\xi_{5\mu}H\gamma_{\mu\nu}\xi_{\mu5}\right) \ , \tag{16}$$

where the same simplifications as in Eq. (15) have been made. Table XIII shows the pattern of mass splittings resulting from this operator. We have assumed that the overall sign of the operator is the same as that of the (net) type-A operator that generated Table XII. Note first that the overall effect on the "centers of gravity" of the $SO(4)$ multiplets (average masses, taking into account multiplicities) is the same as for the type-A operators in Table XII.

The main implication of Table XIII, however, is the pattern of $SO(4)$ violations it predicts.

TABLE XIII: Relative contributions to the masses of heavy-light mesons of given tastes due to the (apparently) dominant type-B operator, Eq. (16).

ξ_5	ξ_{05}	ξ_{i5}	ξ_{ij}	ξ_{i0}	ξ_i	ξ_0	I
-6	-6	-2	-2	+2	+2	+6	+6

In the axial taste multiplet, the spatial component ξ_{i5} is raised relative to the time component ξ_{05}, but this situation is reversed in the tensor and vector multiplets. Furthermore, the absolute value of the time-space taste splitting is the same in each of the three multiplets. This structure is exactly what is observed in Fig. 6. We make the comparison with the lattice data more quantitative in Fig. 7, where the $SO(4)$-breaking mass differences are plotted for the $\bar{l}c$ and $\bar{s}c$ cases. These mass differences have been calculated directly with a jackknife procedure (rather than simply propagating the errors from the differences with the Goldstone meson shown in Fig. 6) in order to take advantage of the correlations to reduce the error in the splittings. In the $\bar{s}c$ case, there is good evidence that the splittings have the sign and relative magnitude predicted in Table XIII. The $\bar{l}c$ case is much noisier, but the signs and magnitudes are at least consistent with expectations. Note also that there is no evidence for a light-mass dependence of the splittings, which is as expected at this order in ASHMχPT.

There is no chiral effective theory to analyze the splittings for heavy-heavy mesons (the $\bar{c}c$ case in Fig. 6). Nevertheless, it is interesting to see that the $SO(4)$ breaking, already clear in the $\bar{s}c$ and $\bar{l}c$ cases, gets very strong in the $\bar{c}c$ case. In particular, the spacings between some members of different $SO(4)$ multiplets (ξ_0 and I, or ξ_{i0} and ξ_i), are smaller than the splittings within multiplets.

VI. THERMALIZATION AND AUTOCORRELATION TIMES

At the start of a new simulation, the system will not be in equilibrium, and gauge configurations generated before it has thermalized should not be included in measurements of physical quantities. The amount of running discarded for thermalization was determined from time histories of the plaquette and chiral condensate, and, when available later, spectrum measurements. The equilibration time varies among the ensembles, and is typically 200
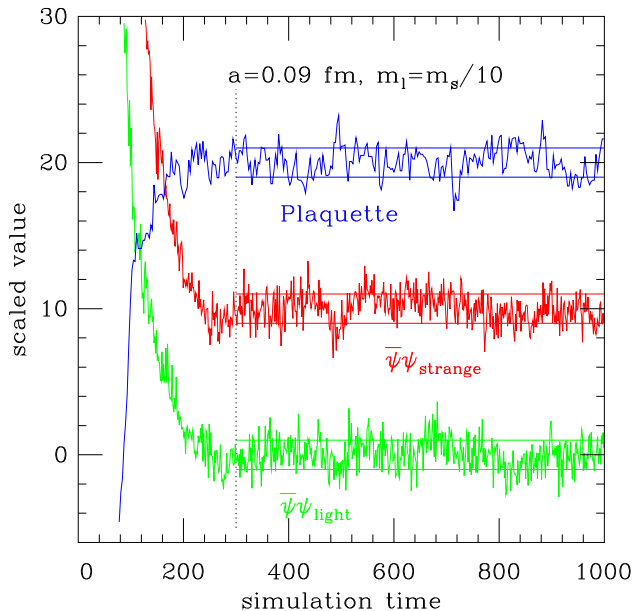
FIG. 8: Equilibration of the plaquette and $\bar{\psi}\psi$ in the ensemble with $a \approx 0.09$ fm and $m_l = m_s/10$. The quantities are rescaled so that their standard deviations, obtained from the equilibrated part of the run, are one, and shifted so that the distributions center at zero, ten and twenty. Horizontal lines for each quantity show the $\pm$ one standard deviation range of the equilibrated quantity, obtained from averaging over simulation times 300 to 6300. (Only the first 1000 time units are shown here.) The vertical line at $T = 300$ shows where we began taking measurements in analysis projects. This particular ensemble was started from a configuration very far from equilibrium, so the warm up effects are dramatic in this plot.

time units, or 300 time units for ensembles starting far from equilibrium. Figure 8 shows the approach to equilibrium in the ensemble with $a \approx 0.09$ fm and $m_l = m_s/10$, which started from a configuration very far from equilibrium.

Because each successive gauge configuration is generated from the previous one *via* a molecular dynamics-based evolution in "simulation time", it will resemble the previous configuration to some degree. This leads to correlations between the values of various observables measured on configurations that are nearby in simulation time. If these correlations are not taken into account, statistical analysis of lattice data will tend to underestimate the errors, since the standard methods for estimating covariance matrices assume that each sample is uncorrelated. We have chosen to save a gauge configuration every five (for $a > 0.09$ fm) or six (for $a \leq 0.09$ fm) units of simulation time, on the grounds that observables mea-

31

sured on configurations separated by less than five units will be so strongly correlated that the small amount of extra information that can be gleaned from them is not worth the effort required to extract it. For many observables, however, five time units is not sufficient separation to eliminate autocorrelations. The choice to save a configuration every five or six time units represents a middle ground: two configurations five units apart differ sufficiently that it is worth saving them both, but are correlated enough that these correlations must be considered when conducting statistical analyses.

We have computed the autocorrelations between the values of various observables on pairs of configurations as a function of the simulation-time separation of the pair. We define the autocorrelation of observable $\mathcal{O}$ at a simulation time separation t as

$$C(\mathcal{O}; t) = \left. \frac{\langle \mathcal{O}_i \mathcal{O}_j \rangle - \langle \mathcal{O}_i \rangle \langle \mathcal{O}_j \rangle}{\langle \mathcal{O}^2 \rangle - \langle \mathcal{O} \rangle^2} \right|_{j=i+t} \tag{17}$$

where the expectation values in the numerator are taken over all pairs of configurations i, j separated by t units of molecular dynamics time. Note that this value is unity by construction for $t = 0$.

This definition suffices for observables like the average plaquette, which has a uniquely measurable value on each configuration. However, we use stochastic estimators to measure the quark scalar condensates. Fluctuations in the measured value of the scalar condensate between different gauge configurations are partly due to physically-meaningful fluctuations of the gauge fields, and partly due to fluctuations in the stochastic estimator. Naïve application of Eq. (17) to such quantities will underestimate the degree of autocorrelation between the scalar condensates on nearby lattices, since the numerator includes extra fluctuations from the variation in the stochastic estimator on different configurations, while the denominator does not.

Fortunately, on many ensembles, we have multiple measurements using different stochastic sources for the condensate. This enables us to disentangle the two sources of fluctuation, by instead defining

$$C(\mathcal{O}; t \neq 0) = \left. \frac{\langle \mathcal{O}_i \mathcal{O}_j \rangle - \langle \mathcal{O}_i \rangle \langle \mathcal{O}_j \rangle}{\langle \mathcal{O}_a \mathcal{O}_b \rangle - \langle \mathcal{O} \rangle^2} \right|_{a \neq b, j=i+t} \tag{18}$$

where a and b are different stochastic sources on the same configuration. (A similar redefinition of the numerator for the $t = 0$ case recovers the result that $C(\mathcal{O}; 0) = 1$.) This method
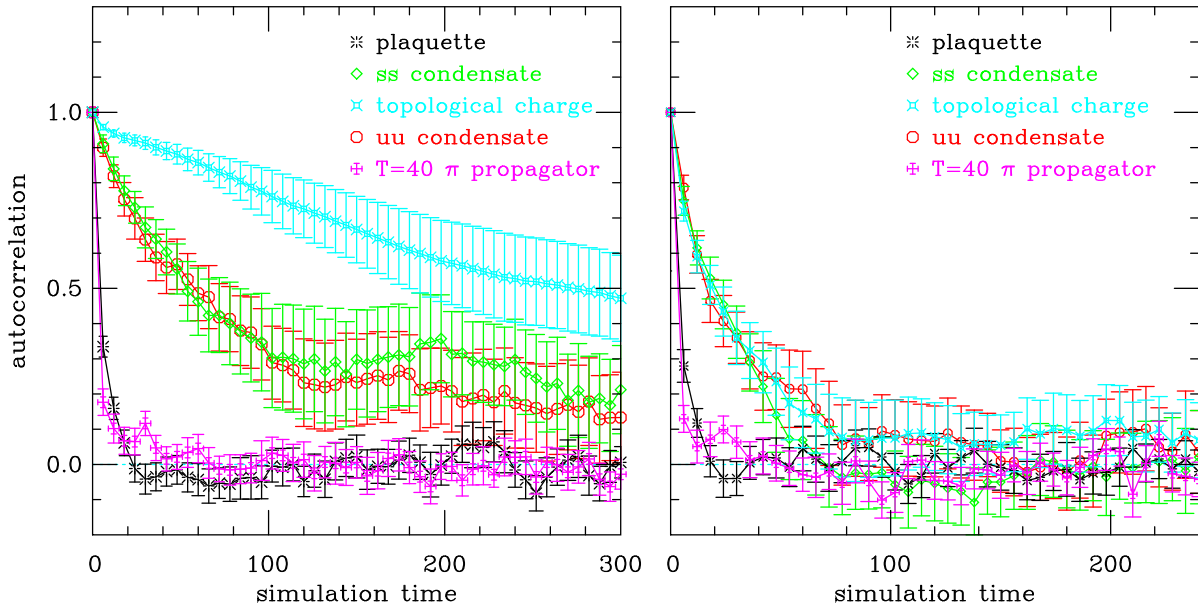
FIG. 9: Autocorrelations of various quantities in simulation time on the ensembles with $m_l = m_s/5$ and $a \approx 0.06$ fm (left) and $a \approx 0.09$ fm (right).

obviously does not apply to ensembles where only a single stochastic source has been run on each configuration.

Figure 9 shows the autocorrelations of several observables in simulation time on two different ensembles. The errors on the autocorrelation at different separations are highly correlated. We present results for the topological charge, the plaquette, the light and strange sea-quark condensates, and the (pseudoscalar) pion propagator at a separation corresponding roughly to the shortest length used in fits to determine M_π. On the finer of these ensembles ($a \approx 0.06$ fm), the topological charge has an extremely long autocorrelation length, followed by the strange- and light-quark condensates; on the coarser one ($a \approx 0.09$ fm), the autocorrelation length of the topological charge is comparable to that of the condensates. The autocorrelation length for the plaquette and the pion propagator are quite short. Nonetheless, even for the pion propagator, there are non-negligible correlations between the propagator on lattices separated by only a few time units, so some blocking procedure is necessary to correctly estimate the covariance matrix for the propagator when performing fits.

We have three gauge ensembles which differ only in their spatial volume. They have $a \approx 0.12$ fm, $m_l = m_s/10$, and lattice volumes of $24^3 \times 64$, $32^3 \times 64$, and $40^3 \times 64$. These
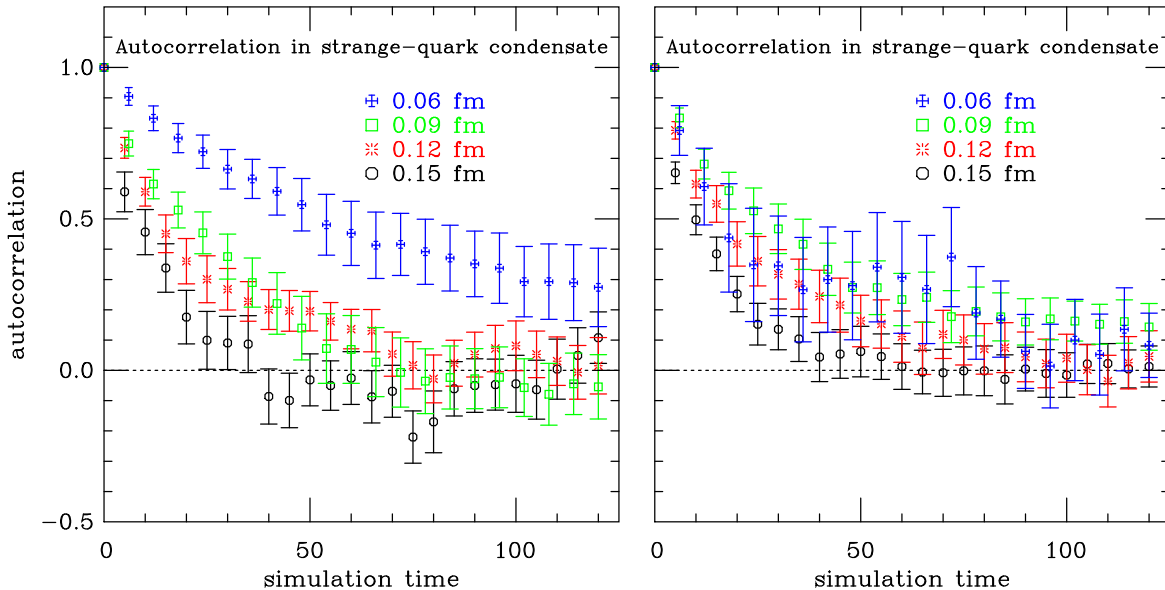
33

FIG. 10: Lattice spacing dependence of autocorrelations in the strange-quark condensate for light sea quark mass $m_l = m_s/5$ (left panel), and $m_l = m_s/10$ (right panel).

ensembles provide us with an opportunity to examine whether the autocorrelation length depends on the lattice volume; we observe no such dependence.

In Fig. 10 we show the autocorrelation function for the strange-quark condensate at four lattice spacings with light quark masses $m_l = m_s/5$ and $m_s/10$. The $m_l = m_s/10$ data suggest a trend toward increasing autocorrelation time with decreasing lattice spacing, although the noisy $a \approx 0.06$ fm data do not fall along that trend. Indeed, the $m_l = m_s/5$ data display this trend more strongly, with a greatly enhanced autocorrelation time for the finest ensemble. The measurements required to do a similar comparison on the physical m_l ensembles have not been completed. Topological charge data are available for all of the $m_l = m_s/5$ ensembles, and a similar trend is apparent there, including a greatly enhanced autocorrelation time for the $a \approx 0.06$ fm, $m_l = m_s/5$ ensemble. It should be noted that the autocorrelation times for this ensemble, particularly for the topological charge, are so long that they create difficulties in estimating the uncertainty in the autocorrelation function.

As discussed in Sec. II, for large lattices there are advantages to using the RHMD algorithm instead of RHMC. Use of RHMD will naïvely result in a decrease of autocorrelation lengths by a factor equal to the Metropolis acceptance rate, generally about 70%. To test for this effect, we compare autocorrelation lengths on the RHMC and RHMD segments of the $a \approx 0.09$ fm, physical light-quark mass ensemble which has roughly an equal number of
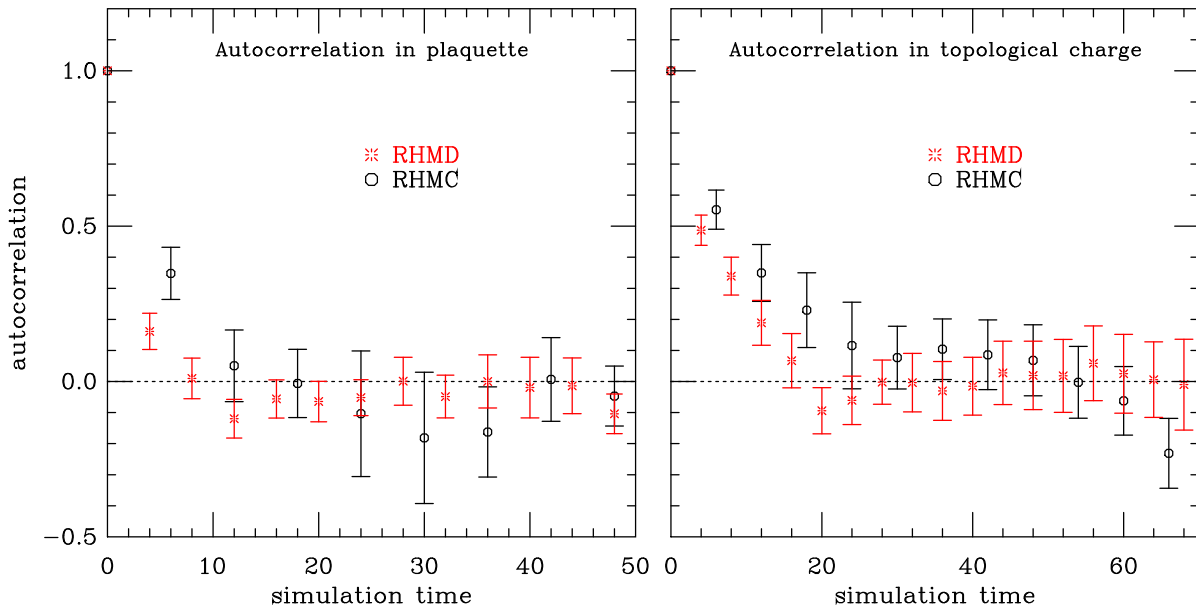
FIG. 11: Dependence of autocorrelation length on whether the Metropolis accept/reject step is present (RHMC) or absent (RHMD) in gauge generation, on the ensemble with $a \approx 0.09$ fm, $m_l = m_s/27$. The left plot shows the plaquette, and the right plot shows the topological charge.

time steps with each algorithm. In anticipation of this decrease in the autocorrelation length we have saved a gauge configuration every four time units in the RHMD evolution, under the assumption that this corresponds approximately to every six time units using RHMC. Such a comparison is shown in Fig. 11. The expected decrease in the autocorrelation length is visible in both the plaquette and the topological charge. It would be natural to do a similar analysis for the strange-quark condensate, as the quantity typically used to probe for thermalization, but those data are too noisy on this ensemble to make any claim about the presence or absence of the expected effect.

VII. CONCLUSIONS

We are nearing completion of the first phase of our project to generate gauge configurations with four flavors of quarks with the HISQ action. In this phase of our effort, we are generating ensembles with four values of the lattice spacing ranging from 0.06 fm to 0.15 fm, and three values of the light quark mass, including the value for which the Goldstone pion mass is equal to the physical pion mass. As can be seen from Tables I and II, we have completed all but three of the planned ensembles with $a \geq 0.06$ fm. We hope to finish

the remaining ones in the coming year. In the second phase of this project we plan additional ensembles at lattice spacings $a \approx 0.045$ fm and 0.03 fm. Most of the HISQ ensembles have been generated using the RHMC algorithm, but we have found that for $a \leq 0.09$ fm, the gauge configurations are smooth enough that one can use the RHMD algorithm, which results in a large savings in computer resources. For $a \leq 0.09$ fm, the RHMD algorithm introduces a systematic error, which is small compared to other uncertainties, and, for all but a few quantities, is smaller than the statistical error. Even for the worst case given in Table VI, the systematic difference between the RHMC and RHMD results is only 1.2 times the statistical error.

We have determined the lattice spacings of the ensembles by two different methods. In one, we extract the Sommer parameter r_1 in lattice units from the heavy-quark potential, and in the other we calculate the leptonic decay constant f_{p4s} of a fictitious pseudoscalar meson with valence quarks of mass $0.4\,m_s$, again in lattice units. Both of these quantities can be determined quickly and accurately for a given ensemble. To obtain the lattice spacing in physical units, we must also determine r_1 or f_{p4s} in physical units using one piece of experimental input. Ultimately, this will be done on the HISQ lattices, but for the moment, we take the physical results for r_1 and f_{p4s} from our more extensive data on the asqtad ensembles. We find excellent agreement between the two approaches.

We have calculated the topological susceptibility on five of the HISQ ensembles, including two with physical mass light quarks, and one with lattice spacing $a \approx 0.06$ fm. We see from Fig. 2 that the simulation samples a wide range of values for the topological charge, and does not appear to become stuck in any sector. The topological susceptibility provides an excellent illustration of the improvement of the HISQ ensembles relative to the asqtad ones, because it is calculated without involving valence quarks. Figure 3 shows this improvement, and also demonstrates the decrease in the susceptibility with pion mass in accordance with the expectation from chiral perturbation theory.

Taste-symmetry breaking for pseudoscalar mesons is discussed in detail in Section V, and a variety of results for it are tabulated in the appendix. We find that the $\bar{ll}$, $\bar{ls}$ and $\bar{ss}$ systems can be understood in terms of SχPT. They all exhibit an accidental $SO(4)$ symmetry, but some small breaking of this symmetry is present in the $\bar{ss}$ system at the coarsest lattice spacing. For the $\bar{lc}$ and $\bar{sc}$ systems, SχPT is not applicable, and the appropriate effective field theory is "all staggered heavy meson chiral perturbation theory," ASHMχPT. $SO(4)$

symmetry is broken, but the pattern of taste splittings can be understood using ASHMχPT. There is no chiral effective theory available to analyze the $\bar{c}c$ system. We see from the data that the breaking of $SO(4)$ symmetry is very strong for this case, but the relative taste splittings are much smaller than in the light meson sector. Indeed, the difference between the RMS pseudoscalar mass and the mass of the taste ξ_5 pseudoscalar (the Goldstone pion in the case of the $\bar{l}l$ system) is 61 Mev, 26 MeV and 19 MeV for the $\bar{l}l$, $\bar{s}s$ and $\bar{c}c$ systems, respectively on the $a \approx 0.12$ fm, $m_l = m_s/5$ ensemble.

We save a gauge configuration every five molecular dynamics time units for ensembles with $a > 0.09$ fm, and every six time units for ensembles with $a \leq 0.09$ fm time units. Successive gauge configurations are, of course, correlated, and these correlations must be taken into account when analyzing the statistical uncertainties of measurements. The autocorrelation length depends on the quantity being measured, the lattice spacing and the light quark mass. A number of examples are given in Sec. VI.

We plan to make these gauge ensembles publicly available, and we believe that they will be useful for the study of a wide range of problems in high energy and nuclear physics.

Acknowledgments

with the U.S. Department of Energy.

Appendix A: Taste splitting of pseudoscalar mesons

In Tables XIV and XV, we tabulate the taste splittings of the pseudoscalar mesons made from combinations of light, strange and charm quarks.

$\approx a$ (fm)	$\gamma_0\gamma_5$	$\gamma_i\gamma_5$	$\gamma_i\gamma_0$	$\gamma_i\gamma_j$	γ_0	γ_i	**1**
			light-light				
0.15	0.1000(71j)	0.1033(8j)	0.1959(29j)	0.1901(57j)	0.2855(46j)	0.2872(114j)	0.3678(441j)
0.12	0.0553(28s)	0.0542(11s)	0.1031(21s)	0.1013(48s)	0.1516(32s)	0.1616(72s)	0.2068(172s)
0.09	0.0180(19j)	0.0180(5j)	0.0335(10j)	0.0328(26j)	0.0493(14j)	0.0485(32j)	0.0631(51j)
0.06	0.0031(5j)	0.0033(1j)	0.0062(2j)	0.0064(6j)	0.0090(3j)	0.0093(7j)	0.0128(7j)
			strange-strange				
0.15	0.0948(14s)	0.1009(12s)	0.1853(19s)	0.1806(19s)	0.2626(24s)	0.2504(29s)	0.3186(50s)
0.12	0.0464(23s)	0.0486(15s)	0.0932(17s)	0.0897(23s)	0.1320(23s)	0.1303(23s)	0.1674(36s)
0.09	0.0212(47s)	0.0157(39s)	0.0283(40s)	0.0315(47s)	0.0386(48s)	0.0458(48s)	0.0601(56s)
0.06	0.0028(10j)	0.0027(1j)	0.0049(4j)	0.0059(11s)	0.0071(4j)	0.0071(5j)	0.0092(6j)
			charm-charm				
0.15	0.3229(25s)	0.5432(27s)	0.7847(33s)	0.6354(27s)	0.9431(37s)	0.8224(33s)	0.9617(41s)
0.12	0.1394(34s)	0.2227(34s)	0.3446(39s)	0.2754(36s)	0.4324(41s)	0.3706(39s)	0.4485(44s)
0.09	0.0486(78s)	0.0719(78s)	0.1129(85s)	0.1000(74s)	0.1410(85s)	0.1355(85s)	0.1748(91s)
0.06	0.0143(21s)	0.0189(3j)	0.0317(6j)	0.0275(21s)	0.0423(7j)	0.0376(6j)	0.0462(7j)

TABLE XIV: Taste splittings for pseudoscalars with equal valence-quark masses on the $m_s/5$ ensembles. These are the splittings for the pseudoscalar mesons with valence quark masses equal to the light sea quark mass, $m_s/5$, equal to the sea strange quark mass, and equal to the sea charm quark mass. For each non-Goldstone taste ξ we tabulate the squared mass difference $r_1^2 a^2 \Delta_\xi = r_1^2(M_\xi^2 - M_5^2)$, where the errors are statistical only. j indicates the error comes from a jackknife analysis, and s indicates the error is just the error from the mass of the non-Goldstone pion. This is a reasonable approximation of the true statistical error in the squared-mass splitting when either (i) the uncertainty in the Goldstone pion mass is much smaller than that of the non-Goldstone pion, and/or (ii) the Goldstone and non-Goldstone pion masses are strongly correlated.

light-charm								
	γ_5	$\gamma_0\gamma_5$	$\gamma_i\gamma_5$	$\gamma_i\gamma_0$	$\gamma_i\gamma_j$	γ_0	γ_i	**1**
γ_5	–	0.088(17)	0.118(17)	0.164(23)	0.137(19)	0.205(29)	0.151(28)	0.185(31)
$\gamma_0\gamma_5$	-0.085(4)	–	**0.031(20)**	0.076(26)	0.049(19)	0.117(30)	0.063(31)	0.097(33)
$\gamma_i\gamma_5$	-0.126(4)	**-0.041(4)**	–	0.045(23)	0.019(20)	0.086(30)	0.033(29)	0.066(35)
$\gamma_i\gamma_0$	-0.205(6)	-0.120(7)	-0.079(6)	–	**-0.027(25)**	0.041(26)	-0.013(24)	0.021(29)
$\gamma_i\gamma_j$	-0.174(5)	-0.088(4)	-0.048(5)	**0.031(8)**	–	0.068(37)	0.014(33)	0.048(35)
γ_0	-0.266(8)	-0.181(8)	-0.140(7)	-0.061(5)	-0.092(10)	–	**-0.054(29)**	-0.020(26)
γ_i	-0.229(7)	-0.144(7)	-0.103(6)	-0.025(5)	-0.056(8)	**0.036(6)**	–	0.034(33)
1	-0.290(8)	-0.205(8)	-0.164(8)	-0.085(6)	-0.116(9)	-0.024(7)	-0.060(6)	–
strange-charm								

TABLE XV: Taste splittings for the heavy-light pseudoscalars on the $a \approx 0.15$ fm $m_s/5$ ensemble. Since the breaking of the approximate $SO(4)$ symmetry is important here, and all the masses are correlated so naive combination of errors is incorrect, we tabulate all of the splittings. As in Table XIV, we tabulate $r_1^2 \left(M_{\xi_2}^2 - M_{\xi_1}^2 \right)$, where ξ_2 and ξ_1 are the tastes in the row and column labels. Since this matrix is antisymmetric, we have placed the light-charm splittings in the upper triangle, and the strange-charm splittings in the lower triangle. All errors are estimated using a jackknife procedure. The $SO(4)$ breaking splittings are shown in **red**.

References

[1] C. Bernard *et al.*, Phys. Rev. D **64**, 054506, (2001), [arXiv:hep-lat/0104002]; C. Aubin *et al.*, Phys. Rev. D **70**, 094505 (2004), [arXiv:hep-lat/0402030]; A. Bazavov *et al.*, Rev. Mod. Phys. **82**, 1349-1417 (2010), [arXiv:0903.3598].

[2] E. Follana *et al.*, Nucl. Phys. B, Proc. Suppl. **129** and **130**, 447 (2004), [arXiv:hep-lat/0311004].

[3] E. Follana *et al.*, Nucl. Phys. B, Proc. Suppl. **129** and **130**, 384, 2004, [arXiv:hep-lat/0406021].

[4] The HPQCD/UKQCD Collaboration: E. Follana *et al.*, Phys. Rev. D **75**, 054502 (2007), [arXiv:hep-lat/0610092].

[5] The HPQCD/UKQCD Collaboration: E. Follana *et al.*, Phys. Rev. Lett. **100**, 062002 (2008), [arXiv:0706.1726].

[6] The HPQCD/UKQCD Collaboration: I. Allison *et al.*, Phys. Rev. D **78**, 054513 (2008), [arXiv:0805.2999].

[7] The HPQCD/UKQCD Collaboration: C. Davies *et al.*, Proc. Sci., LATTICE2008 **(2008)** 118, [arXiv:0810.3548].

[8] The HPQCD Collaboration: H. Na, C.T.H. Davies, E. Follana, G.P. Lepage, and J. Shigemitsu, Phys. Rev. D **82**, 114506 (2010), [arXiv:1008.4562].

[9] The HPQCD Collaboration: E.B. Gregory *et al.*, Phys. Rev. D **83**, 014506 (2011), [arXiv:1010.3848].

[10] The HPQCD Collaboration: C.T.H. Davies, E. Follana, G.P. Lepage, H. Na and J. Shigemitsu, Phys. Rev. D **82**, 114504 (2010), [arXiv:1008.4018].

[11] The HPQCD Collaboration: C.T.H. Davies *et al.*, Phys. Rev. Lett. **104**, 132003 (2010), [arXiv:0910.3102].

[12] the HPQCD collaboration: H. Na, C.T.H. Davies, E. Follana, G.P. Lepage, and J. Shigemitsu, [arXiv:1206.4936].

[13] HPQCD Collaboration: H. Na *et al.*, Phys. Rev. D **82**, 114506 (2010), [arXiv:1008.4562]; Proc. Sci., LATTICE2011 **(2011)** 286, [arXiv:1111.0225].

[14] The MILC Collaboration: A. Bazavov *et al.*, Phys. Rev. D **82**, 074501 (2010), [arXiv:1004.0342].

[15] K. Symanzik, In: Recent Developments in Gauge Theories, edited by G. 't Hooft *et al.*, (Plenum Press, New York, 1980), p. 313, (1980); K. Symanzik, Nucl. Phys. **B226**, 187 (1983); M. Lüscher and P. Weisz, Phys. Lett. B **158**, 250 (1985); M. Lüscher and P. Weisz, Commun. Math. Phys. **97**, 59 (1985); M.G. Alford *et al.*, Phys. Lett. B **361**, 87 (1995).

[16] The MILC Collaboration: A. Bazavov, *et al.*, arXiv:1301.5855.

[17] E. Follana, A. Hart and C.T.H. Davies (HPQCD Collaboration), Phys. Rev. Lett. **93**, 241601 (2004); S. Dürr and C. Hoelbling, Phys. Rev. D **69**, 034503 (2004); S. Dürr, C. Hoelbling and U. Wenger, Phys. Rev. D **70**, 094502 (2004); G. C. Donald, C.T.H. Davies, E. Follana, A.S. Kronfeld, Phys. Rev. D **84**, 054504 (2011).

[18] C. Bernard, Phys. Rev. D **73**, 114503 (2006); C. Bernard, M. Golterman, Y. Shamir, and S.R. Sharpe, Phys. Lett. B **649**, 235 (2007); Y. Shamir, Phys. Rev. D **71**, 034509 (2005); and

Phys. Rev. D **75**, 054503 (2007); C. Bernard, M. Golterman, Y. Shamir, and S.R. Sharpe, Phys. Rev. D **77**, 114504 (2008); David H. Adams, Phys. Rev. D **77**, 105024 (2008).

[19] R. Sommer, Nucl. Phys. **B411**, 839 (1994), [hep-lat/9310022].

[20] C. Bernard *et al.*, Phys. Rev. D **62**, 034503 (2000), [arXiv:hep-lat/0002028].

[21] The HPQCD Collaboration: C.T.H. Davies *et al.*, Phys. Rev. D **81**, 034506 (2010), [arXiv:0910.1229].

[22] Zh. Hao *et al.* Phys. Rev. D **76**, 034507 (2007), [arXiv:0705.4660]; A. Hart, G. von Hippel and R.R. Horgan, Phys. Rev. D **79**, 074008 (2009), [arXiv:0812.0503].

[23] M.A. Clark and A.D. Kennedy, Nucl. Phys. Proc. Suppl. **129**, 850 (2004), [arXiv:hep-lat/0309084]; M.A. Clark and A.D. Kennedy, Phys. Rev. D **75**, 011502 (2007), [arXiv:hep-lat/0610047]; M.A. Clark and A.D. Kennedy, Phys. Rev. Lett. **98**, 051601 (2007), [arXiv:hep-lat/0608015].

[24] J.C. Sexton and D.H. Weingarten, Nucl. Phys. **B380**, 665 (1992).

[25] I.P. Omelyan, I.M. Mryglod, and R. Folk, Phys. Rev. E **65**, 056706 (2002); T. Takaishi and Ph. de Forcrand, Phys. Rev. E **73**, 036706 (2006), [arXiv hep-lat/0505020].

[26] A. Bazavov *et al.*, Proc. Sci., LATTICE2010 **(2010)** 074, [arXiv:1012.0868].

[27] H. Leutwyler and A.V. Smilga, Phys. Rev. D **46**, 5607 (1992).

[28] The MILC Collaboration: A. Bazavov *et al.*, Phys. Rev. D **81** 114501 (2010), [arXiv:1003.5695].

[29] T.A. DeGrand, A. Hasenfratz, and T.G. Kovacs, Nucl. Phys. **B505**, 417 (1997), [arXiv:hep-lat/9705009].

[30] A. Hasenfratz and C. Nieter, Phys. Lett. B **439**, 366 (1998), [arXiv:hep-lat/9806026].

[31] A. Hasenfratz and F. Knechtli, Phys. Rev. D **64**, 034504 (2001), [arXiv:hep-lat/0103029].

[32] M. Lüscher, Phys. Lett. B **593**, 296 (2004), [arXiv:hep-th/0404034].

[33] C. Davies *et al.*, Nucl. Phys. Proc. Suppl. **119**, 595 (2003), [hep-lat/0209122].

[34] G. P. Lepage and P. B. Mackenzie, Phys. Rev. D **48**, 2250 (1993), [hep-lat/9209022].

[35] S. J. Brodsky, G. P. Lepage and P. B. Mackenzie, Phys. Rev. D **28**, 228 (1983).

[36] W. Lee and S. Sharpe Phys. Rev. D **60**, 114503 (1999), [arXiv:hep-lat/9905023].

[37] C. Aubin and C. Bernard, Phys. Rev. D **68**, 034014 (2003), [arXiv:hep-lat/0304014] and Phys. Rev. D **68**, 074011 (2003), [arXiv:hep-lat/0306026].

[38] J. Komijani and C. Bernard, Proc. Sci., LATTICE2012 **(2012)** 199, [arXiv:1211.0785];

C. Bernard and J. Komijani, in preparation.